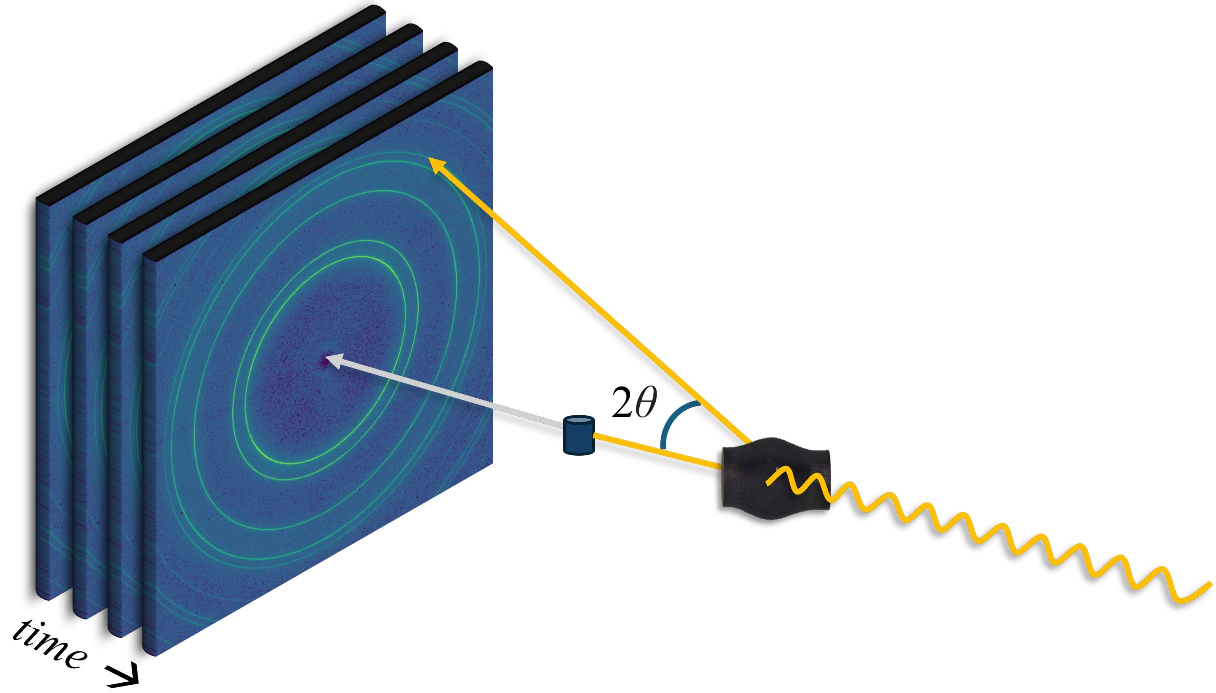

Tracking meta-dynamic recrystallization in a Ni-based superalloy using time-resolved synchrotron X-ray diffraction

Master Thesis Project

LOVISA ÅKESSON

DEPARTMENT OF PHYSICS

CHALMERS UNIVERSITY OF TECHNOLOGY
Gothenburg, Sweden 2025
www.chalmers.se

Master's thesis 2025

Tracking meta-dynamic recrystallization in a Ni-based superalloy using time-resolved synchrotron X-ray diffraction

LOVISA ÅKESSON

Department of Physics
Division of Microstructure Physics
Chalmers University of Technology
Gothenburg, Sweden 2025

Tracking meta-dynamic recrystallization in a Ni-based superalloy using time-resolved synchrotron X-ray diffraction
LOVISA ÅKESSON

Supervisor: Magnus Hörnqvist Colliander
Examiner: Magnus Hörnqvist Colliander

Master's Thesis 2025
Department of Physics
Division of Microstructure Physics
Chalmers University of Technology
SE-412 96 Gothenburg
Telephone +46 31 772 1000

Cover: schematic illustration of *in situ* X-ray diffraction.

Typeset in LaTeX
Printed by Chalmers Reproservice
Gothenburg, Sweden 2025

Tracking meta-dynamic recrystallization in a Ni-based superalloy using time- resolved synchrotron X-ray diffraction
LOVISA ÅKESSON
Department of Physics
Chalmers University of Technology

Abstract

The drive towards more sustainable aviation has gained traction as the global aviation industry expands alongside increasing demands to reduce carbon emissions. This drive has pushed research in materials science aimed at developing alloys capable of withstanding high operating temperatures while maintaining metallurgical stability. The nickel-based superalloy Haynes 282 has emerged as a promising material for use in aero-engine applications. Recrystallization plays a critical role in determining the final microstructure and, consequently, the mechanical properties of metallic materials. This project aims to develop computational methods for studying the dynamics of meta-dynamic recrystallization in Haynes 282, to gain a deeper understanding of how the recrystallization process evolves.

The superalloy samples were first deformed at elevated temperatures. Right after the deformation stopped, *in situ* synchrotron X-ray diffraction (XRD) measurements were performed while maintaining the constant deformation temperature. Diffraction patterns were recorded as a function of time. A method was developed to separate the signal into contributions from the deformed and recrystallized grains. This enabled the calculation of the recrystallized fraction, and the tracking of recrystallized grain evolution over time. These analyses were applied to samples deformed at different temperatures. For the sample deformed at 1100 °C, the recrystallized fraction increased rapidly, from an initial average of approximately 5 % to 90 % within 120 seconds. Higher deformation temperatures resulted in faster recrystallization kinetics and higher final fractions. The progression of new grains and their size distribution was also studied, showing an increase in both the number of grains and their average size over time.

The results were compared to previous experimental measurements of Haynes 282, where electron backscatter diffraction was used to quantify the recrystallization and grain growth. The findings of this project align with conclusions previously drawn. The methodology developed in this work demonstrates that time-resolved synchrotron XRD data can be used to effectively study recrystallization, enabling high temporal resolution and potentially greater sensitivity to small grains.

Keywords: dynamic recrystallization, meta-dynamic recrystallization, Ni-base superalloys, synchrotron, XRD

Acknowledgements

Throughout this work, I have had the honour of learning, exploring my own ideas, being challenged, and having fun, all while continuously being supported. I would like to express my deepest gratitude to my supervisor, Prof. Magnus Hörnqvist Colliander, for making this possible. It has been a true pleasure to learn from you and work with you, and I sincerely hope our paths will cross again in the future.

I am also grateful to my friends and family for their interest in the project and for their continuos support. Thank you as well to the new friends I have made along the way. I would like to thank Chalmers University of Technology for the knowledge, inspiration, and countless opportunities offered throughout my Bachelor's and Master's studies, and for being my second home during these years. Finally, I gratefully acknowledge the financial support from Jernkontoret and the Neutron and X-ray Science for Industrial Technology Transitions, which supported this research.

Lovisa Åkesson, Gothenburg, May 2025

List of Acronyms

Below is the list of acronyms that have been used throughout this thesis listed in alphabetical order:

cDRX	continuous dynamic recrystallization
dDRX	discontinuous dynamic recrystallization
DRV	dynamic recovery
DRX	dynamic recrystallization
EBSD	electron backscatter diffraction
fcc	face-centered cubic
$f_{\mathbf{RX}}$	recrystallized fraction
FWHM	full width at half maximum
gDRX	geometric dynamic recrystallization
HAGB	high angle grain boundaries
HT	heat treatment
KDE	kernel density estimation
LAGB	low angle grain boundaries
mDRX	meta-dynamic recrystallization
pDRX	post-dynamic recrystallization
RX	recrystallization
SEM	scanning electron microscopy
γ_{SFE}	stacking fault energy
TMP	thermomechanical processing
XRD	X-ray diffraction

Contents

List of Figures

List of Tables

1

Introduction

As the global aviation industry continues to grow, there is increasing pressure to develop aircraft that not only meet higher performance standards but that also reduces their environmental impact. In 2022, emissions from the aviation industry accounted for between 3.8 to 4 % of the total green house gas emissions from the European Union [1]. The drive for developing more sustainable aviation is essential to addressing global challenges such as fuel consumption and carbon emissions. Enhancing the performance of aircraft engines is a promising approach to achieve these goals. The efficiency of an engine's core is largely dependent on the maximum operating temperature, which is controlled by the metallurgical stability of the materials used in the hot sections of the engine [2].

Nickel-based superalloys are a class of metals able to operate at temperatures near their melting point, offering a balance between high-temperature resistance and mechanical performance [3]. In addition, these alloys stand out because of their long fatigue life and their resistance to oxidation and corrosion. One such Ni-based superalloy engineered for high-temperature structural applications is Haynes 282, specifically developed with properties that make it a suitable material for critical gas turbine applications [4].

Because of their high mechanical strength, superalloys need be formed into their final shape at high temperatures. During hot deformation, these alloys develop a microstructure with a high dislocation density, which results in increased internal energy and mechanical strength, but reduced ductility and thermal stability. Such deformed structures can also exhibit a decreased creep resistance due to the created dislocations that act as fast diffusion pathways. To achieve the desired mechanical properties, it is often necessary to restore a more stable microstructure, usually with equiaxed grains, through recrystallization. In this process, deformed grains are replaced with new, strain-free grains. The grain size resulting from recrystallization is particular critical, as smaller grains generally enhance strength and resistance to crack initiation, but larger grains may provide better resistance to creep and crack propagation.

In typical thermomechanical processing (TMP) of superalloys, dynamic recrystallization (DRX) occurs during the deformation, and meta-dynamic recrystallization (mDRX) often follows during the cooling phase post the deformation, especially in large components where cooling is slower. As a result, the final microstructure of these alloys is usually recrystallized. However, once the recrystallization is complete, the grains can only evolve further by increasing in size. If the recrystallized grains are too large, they cannot be made smaller again without another full processing cycle. Therefore, understanding the kinetics of recrystallization is essential for controlling the grain size and optimizing the material performance.

1.1 Previous Experimental Work

Eriksson et al. [5] has previously studied the process of recrystallization in Haynes 282. In their work, different samples were deformed and held at the deformation temperature for different time ranges, before being quenched. The alloy samples were then sectioned along the compression direction, and a scanning electron microscope (SEM) was used to perform electron backscatter diffraction (EBSD) analysis of each sectioned sample. The classification of deformed and recrystallized grains was made based on variations of crystallographic orientations within each grain, which is related to the dislocation density. In this way, information about the f_{RX} and grain size evolution of the recrystallized grains was obtained. This *ex situ* method allowed for single time-instances during the recrystallization process to be studied. However, questions about if the quenching or sample-to-sample variations can have affected the microstructure studied remain. In addition to this, finding a technique which captures the dynamics of the microstructural evolution with higher temporal resolution and with higher sensitivity to smaller grains is needed, to help explain the results obtained from the EBSD measurements and to gain an even deeper understanding of the recrystallization process.

1.2 Aim of the Project

To overcome the limitations of *ex situ* methods, *in situ* techniques such as synchrotron based X-ray diffraction (XRD) can be used. This method enables non-destructive, time-resolved measurements of a single sample throughout the recrystallization process. The diffracted signal from such measurement contains information about the whole sample volume analysed, including contributions from both the deformed and the recrystallized grains. One challenge with these measurements remains: there is currently no established method for separating and quantifying the respective contributions from the deformed and recrystallized grains. There is therefore a need for developing a robust and general method which enables such separation, thereby allowing for more detailed insights into the dynamics of recrystallization.

The aim of this thesis is to track mDRX in the Ni-based superalloy Haynes 282, by developing computational methods for processing time-resolved synchrotron XRD data. Previously collected *in situ* synchrotron data from high temperature deformation experiments will be used for developing these methods. The programming language Python will be used for processing and analysing the obtained diffractograms. Using the developed methods, key parameters such as the recrystallized fraction, the number of recrystallized grains, and the grain size evolution are aimed to be evaluated over time. This project further aims to apply these methods to samples deformed at different temperatures, to analyse the influence of temperature on the recrystallization kinetics. Lastly, the project aims to evaluate the obtained results in a comparison with the EBSD measurements previously performed of the superalloy by Eriksson et al. [5]. In this way, this project aims to evaluate the use of *in situ* synchrotron XRD measurements for studying recrystallization in and beyond superalloys.

2

Theoretical Background

This chapter covers the underlying theory of the material and methods studied. It starts with an introduction to thermochemical processing of superalloys. Descriptions of XRD and *in situ* synchrotron measurements are then covered.

2.1 Theromechanical processing of superalloys

Ni-based superalloys are among the most commonly used materials in turbo engines. These stand out from other metallic alloys because of their high creep strength and oxidation resistance, enabling Ni-based superalloys to be used at over 70% of their melting temperature [6]. In addition to their high temperature performance, Ni-based superalloys typically exhibit low to medium stacking fault energy (γ_{SFE}), which influences their deformation behaviour. Haynes 282 is a wrought Ni-based superalloy, designed to possess a combination of excellent weldability and high creep resistance, making it a suitable material for high temperature structural applications such as aero and industrial gas turbine engines [4].

Ni-based superalloys are commonly shaped using TMP, through either a sequential or simultaneous combination of plastic deformations and thermal processes [7]. Examples of TMP include forging and hot rolling, where the alloy is subjected to high forces during elevated temperatures. Plastic deformation during TMP occurs through the nucleation and propagation of line defects in the crystals. These defects are called dislocations, and propagate on specific atomic planes. As the deformation progresses, the number of dislocations accumulates in the structure. The increased dislocation density makes the material harder but less ductile, and the associated increased stored energy makes the microstructure less thermally stable. During TMP, the distribution of temperature and plastic deformation is typically not uniform, and so the resulting dislocation density varies in the deformed material. After TMP, the material can be exposed to heat treatment (HT), to further refine the microstructure.

The main phase of the Haynes 282 superalloy is the austenitic γ phase, characterized by a face-centered cubic (fcc) crystal lattice, and a γ'-phase is used as a strengthening precipitate [7]. Primary carbides, usually in the form of intragranular phases, nucleate during solidification of the alloy, and secondary carbides, usually intergranular phases, nucleate during HT. The γ' phase of Haynes 282 has a melting temperature below the temperature used for TMP. In this report, data from TMP experiments will be analysed, meaning that the microstructure studied is of the primary γ phase. The HT can thereafter be used to precipitate the secondary strengthening phase, as well as to nucleate the secondary intergranular carbides used for preventing grain boundary sliding to improve creep resistance. The final HT can thus be designed to tailor the microstructure of the alloy to best suit the area of application.

2.2 Recovery and recrystallization

The increase in interface and dislocation density during the TMP makes the material less thermodynamically stable [8]. To reduce the free energy in the material, thermally activated processes can be initiated either during or after the deformation to remove the defects. Two such processes occurring during TMP are dynamic recovery (DRV) and DRX. Their static counterparts are what cause the microstructure reconstitution post TMP. During recovery, the moving dislocations can rearrange into lower energy structures such as low angle grain boundaries (LAGB), and they can also annihilate with other dislocations, effectively cancelling out their contribution to the stored energy. The rate of recovery is material specific and depends on factors such as γ_{SFE}. Materials with low γ_{SFE} tend to resist recovery, as this process requires dislocations to change slip planes, a mechanism known as cross-slip. A low γ_{SFE} increases the energy barrier for cross-slip, making it more difficult for dislocations to rearrange and annihilate. As a result, dislocations are instead more likely to form stacking faults or deformation twins. When recovery is hindered in this way, the accumulated dislocation density may instead lead to the onset of recrystallization.

The process of recrystallization has been defined as "the formation of a new grain structure in a deformed material by the formation and migration of high angle grain boundaries (HAGB) driven by the stored energy of deformation" [9]. The nucleation of new grains is governed by the reduction in stored energy in the material, and the grain growth by reduction in energy related to the grain boundaries. The point of nucleation and growth of the new grains during deformation can either be clearly distinguishable, referred to as discontinuous dynamic recrystallization (dDRX), or it can occur uniformly through the material with no clear stages of nucleation and growth, called continuous dynamic recrystallization (cDRX). Materials with low γ_{SFE} generally exhibit dDRX. If the material does not recrystallize fully during the deformation, it can continue on afterwards, if the material is kept at a temperature above the recrystallization temperature. The general term for this type of recrystallization occurring after deformation is mDRX (sometimes also referred to as post-dynamic recrystallization (pDRX)). During mDRX, recrystallized grains nucleated during the deformation can continue to grow in size. Previous experiments on Ni-based superalloys have shown that nucleation of new grains can also occur post deformation, usually following an incubation time ranging from several seconds to minutes [10][11][12].

Figure 2.1 shows EBSD images of different stages during a mDRX process [5]. These samples were first deformed to a strain of 0.2 at a temperature of 1080 °C. After the deformation, the samples were held at the same deformation temperature for either 0, 5 or 15 seconds as shown in (a), (b) and (c) respectively. The gray grains in the images are deformed grains, and the red are recrystallized. As visible, the deformed grains are large in size and typically elongated. The recrystallized grains are more equiaxed and initially small, but can grow in size as the recrystallization progresses.

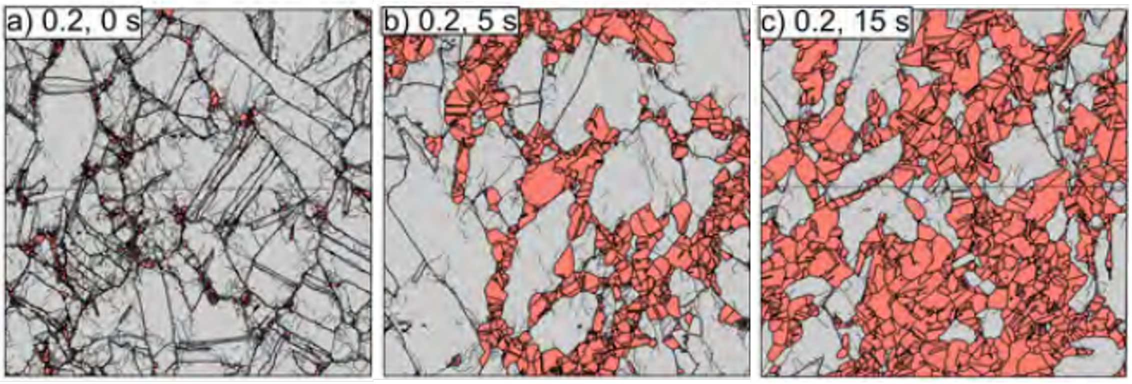

Figure 2.1: Example of EBSD maps showing the progression of mDRX for samples deformation to a strain of 0.2, and thereafter held at 0, 5 and 15 seconds. The gray areas indicate deformed grains and red recrystallized grains.

DRX is a thermally activated process and is therefore strongly influenced by temperature. Its kinetics follow an Arrhenius-type relationship, meaning that even small changes in deformation temperature can lead to significant changes in the recrystallization rate [13]. The rate of f_{RX} also depends on the dislocation density, since a higher density corresponds to a greater stored internal energy, which drives the recrystallization process.

2.3 X-ray diffraction

One technique for studying microstructural evolution in crystalline materials is XRD [14]. In this technique, an X-ray beam is sent towards a sample material. The interaction between the beam and the electrons in the sample results in scattering of the X-rays, where the angle of diffraction relative to the incident beam gives information about the crystalline structure. The wavelength of X-rays is of similar order as atomic spacing, meaning that diffraction is affected by the spacing of atoms. A lot of the diffracted rays will interfere destructively, resulting in diminished amplitudes, while others will interfere constructively. The constructive interference occurs if the phase difference between the diffracted rays from different lattice planes is a multiple of 2π. This interference can be described by Bragg's law, which relates the spacing between the lattice planes (d), the wavelength of the incident X-ray beam (λ) and the diffraction angle (θ), as shown in Equation (2.1):

$$n\lambda = 2d\sin(\theta), \tag{2.1}$$

where n is an integer. The principle of constructive interference according to Bragg's law is shown in Figure 2.2.

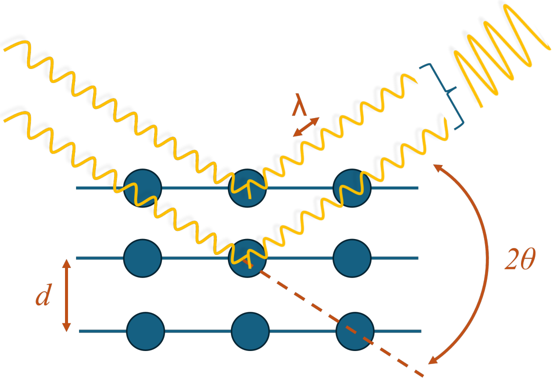

Figure 2.2: Schematic illustrating the principle of Bragg's law. The X-ray with wavelength λ and incident angle θ scatters from interaction with electrons. Constructive interference occurs between rays scattered from the lattice planes of interplanar spacing d.

The diffraction pattern from the scattered rays will thus be a result of the distance between the diffracting planes. Diffraction from a specific family of planes in a grain occurs when the grain is oriented such that the planes fulfil the Bragg condition. For a material with randomly oriented grains, the scattered rays will form a circular diffraction pattern with a radius of 2θ around a centre on a two-dimensional detector image. This is illustrated in Figure 2.3, where a diffraction pattern of green rings is visible on a blue background. The rings in an XRD pattern are referred to as Debye-Scherrer rings. A two-dimensional detector image is often separated into an azimuthal (χ) and a 2θ direction, as marked in Figure 2.3. The azimuthal direction is circular around the image centre, while the 2θ goes from the centre and outwards.

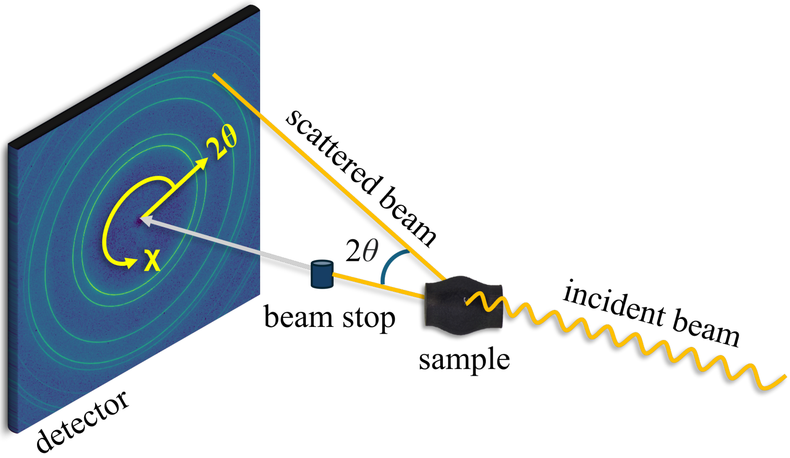

Figure 2.3: Schematic illustration of how an XRD pattern is created on a two-dimensional detector. The incident beam scatters with an angle 2θ, which produces intensity spots around a ring on the detector image. A beam-stop is used to avoid measuring the high intensity of the non-scattered beam.

2.3.1 Synchrotrons and the power of *in situ* measurements

XRD can be studied using laboratory based X-ray sources. However, the relatively low energy of laboratory sources limits the penetration depth to just a few micrometres, such that only near surface regions of samples can be studied [15]. In addition, the low photon flux typically results in long measuring times. To overcome the limitations of laboratory X-ray sources, a synchrotron facility can be used. A synchrotron is a kind of cyclic particle accelerator, where an electron beam is accelerated to a high constant speed around a closed loop using sequences of magnets to reach speeds close to the speed of light [16]. When charged particles are subjected to an acceleration perpendicular to their velocity, they emit electromagnet radiation referred to as synchrotron radiation, which is a high-intensity spectrum of X-rays. The synchrotron radiation can be generated with very high energy, and extremely high flux many orders of magnitude higher than laboratory sources. The X-rays emitted by the electrons are directed into beam lines adjacent to the circular loop. Measuring equipment are located at the end of each beam line, using the X-rays for various experiments such as XRD.

An alternative way of studying recrystallization is to use an electron microscope, such as a SEM. EBSD is a SEM technique, and is one of the major reference techniques for studying recrystallization [17]. Other techniques include mechanical hardness testings, where the decrease in strength of the sample material is connected to the reduction in dislocation density as an effect of the recrystallization. Microscopy and mechanical techniques are often conducted *ex situ*, where samples subjected to heat treatment are quickly quenched to interrupt any ongoing recrystallization before being analysed. The cooling might alter the microstructural change aimed to be analysed, and it might be difficult to accurately conduct experiments within precise time frames. To study the time evolution of recrystallization, a new sample might be required for each time step during the process. This opens up for sample specific defects which makes the process more difficult to study.

To study the dynamics of processes, *in situ* techniques are often preferred, as they allow for non-destructive measurements. Physical properties such as relative permeability and resistivity tend to change with microstructural changes, and can thus serve as indirect *in situ* measures of recrystallization. However, these signals are also affected by recovery processes, making it challenging to isolate the specific contribution from recrystallization. Furthermore, the interpretation of signals from such properties can be complex or subjective. *In situ* synchrotron XRD allows for tracking of individual grains in real time, making it a promising technique for studying the dynamics of recrystallization of a single sample with high resolution non-destructively.

2.3.2 XRD diffractograms of deformed fcc crystals

The diffraction images obtained from XRD measurements consist of high-intensity spots, emerging as an effect of diffraction from single grains oriented in the direction of the plane diffracted from [17][18]. In so called powder diffraction, many crystals with random orientations contribute to the observed diffraction, and the large number of diffraction spots overlap and create the continuos Debye-Scherrer rings. The amplitude and phase of the scattered X-rays can be described mathematically by the structure factor F_{hkl}, where hkl are Miller indices. For an fcc crystal, F_{hkl} is only non-zero if hkl are either all even or all odd. This means that the four first diffracted planes visible in an XRD diffractogram from an fcc are (in the order from highest to lowest d): 111, 200, 220 and 311. Note that the multiplicity factor for each set of planes, i.e. the number of equivalent planes due to symmetry, differs. Out of the planes listed, the $\{311\}$ set has the highest multiplicity of 24, while $\{200\}$ has the lowest multiplicity of six.

During mechanical deformation, the grains will rotate due to the movement of dislocations in the lattice [19]. The crystal orientation will shift such that the grains orient towards an ideal direction. This direction depends on multiple factors such as the crystal structure and mode of deformation. The distribution of crystal orientations is referred to as texture. A crystal system in which the grains are randomly oriented has no texture, whereas a system with preferred directions has texture. For a deformed material, the texture can be prominent in an XRD pattern. The crystal symmetry of a deformed material causes the intensity around a Debye-Scherrer ring to vary rather than being uniform. Instead of a constant intensity, distinct maxima and minima appear at specific azimuthal angles. The positions of these intensity variations depend on the crystal structure, the orientation of the applied deformation force, and the specific Debye-Scherrer ring analysed. In addition, the diffracted signal from the elongated deformed grains will appear arcs on the diffraction image, in contrast to the more discrete spots produced by recrystallized grains. The arcs from many grains overlap to form the Debye-Scherrer rings.

3

Methods

This chapter covers the methodology of the project. It begins with explaining the experimental procedure, conducted prior to the start of this project. This explanation is then followed by a more in-depth description of the written computational functions.

3.1 Experimental set-up and XRD measurements

The experimental measurements were conducted prior to the start of this project by the PhD candidate Emil Eriksson. The Haynes 282 samples were prepared as cylindrical bodies of length 10 mm and diameter of 4 mm. The XRD measurements were performed at the third generation synchrotron source Petra III at DESY in Germany, using the experimental hutch EH3 at the beamline P07 [20]. The measurements were conducted using the dilatometer DIL 805A/D by TA instruments, designed for quenching experiments with the possibility to deform samples using compression [21]. The samples were heated using induction coils, and the temperature was measured using a thermocouple welded onto each sample. For each individual experiment, the sample was held horizontally between two anvils, and the compression was made by applying a force F onto one of the anvils, moving it a distance δ towards the other anvil. Figure 3.1 illustrates the sample, where Figure 3.1a shows a schematic of the compression, and Figure 3.1b shows an example of a deformed sample, where the strain induced compression reduced the sample length from 10 to 7.5 mm. The welding residues from the mounted thermocouple is visible at the centre of the sample. The samples were heated to a range of different temperatures, and were compressed to varying strain levels and strain rates. In this report, datasets of heating temperatures 1080, 1100 and 1020 °C, a strain of 0.3, and a strain rate of $0.05\,\mathrm{s}^{-1}$ are analysed.

The sample was mounted at a distance of 1.68 m from the detector (the exact distance was calibrated by LaB6 standards). The detector consisted of 2048 by 2048 pixels, each of a size of 200 μm. The beam was directed perpendicular to the applied force, such that it passed through centre of the sample visible in Figure 3.1b. The X-ray beam had a size of 400 by 400 μm with a wavelength of 0.1204 Å and equivalent energy of 103 keV. At the end of the deformation, the moving anvil was kept at the deformation distance δ and the temperature was kept constant, allowing for the mDRX to occur. The fast data acquisition started right after the deformation finished. XRD data was acquired every 0.1 s for 120 s. The data at every time instance was saved in a tag image file format (tif) file.

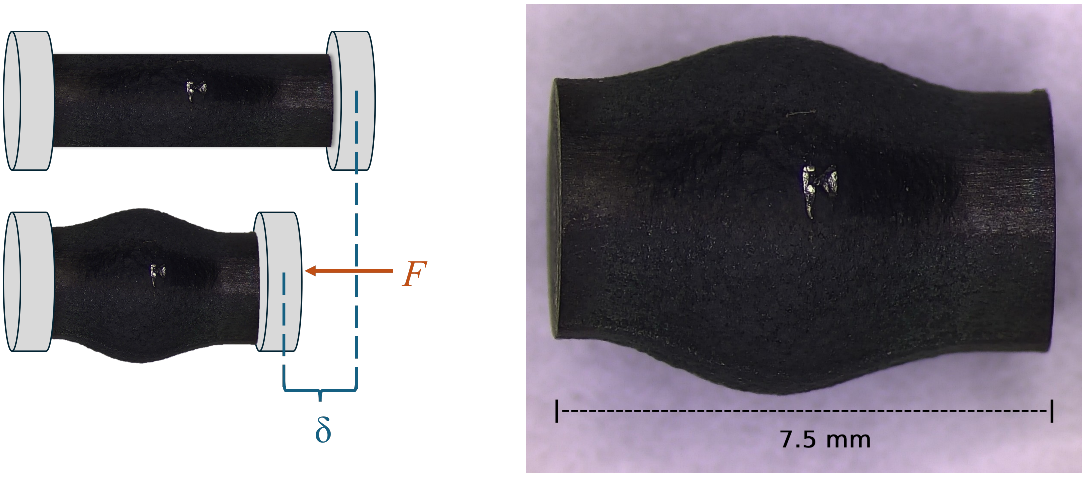

(a) **(b)**

Figure 3.1: Illustration of the deformation of the sample, (a) showing a schematic of a sample being held and compressed between two anvils and (b) showing an actual image of a compressed sample.

The induced strain of 0.3 indicates the maximum strain in the sample. In reality, the distribution of strain throughout the sample varies. Figure 3.2 shows an example of a strain map of a deformed Ni-based superalloy, where the coloured areas indicate the magnitude of the effective strain. The figure is recreated from [22]. Note that the forging direction is vertical in this example, as indicated by the arrow in the figure. In the experiments performed in this thesis, the X-rays would pass in the horizontal direction in the equivalent strain map. The beam therefore passes through volumes of varying strains. As visible, at the centre of the sample in the example figure, the effective strain has a value of approximately 1.15 mm/mm, whereas the left and right boundaries have values of approximately 0.6 mm/mm — less than half the magnitude of the centre.

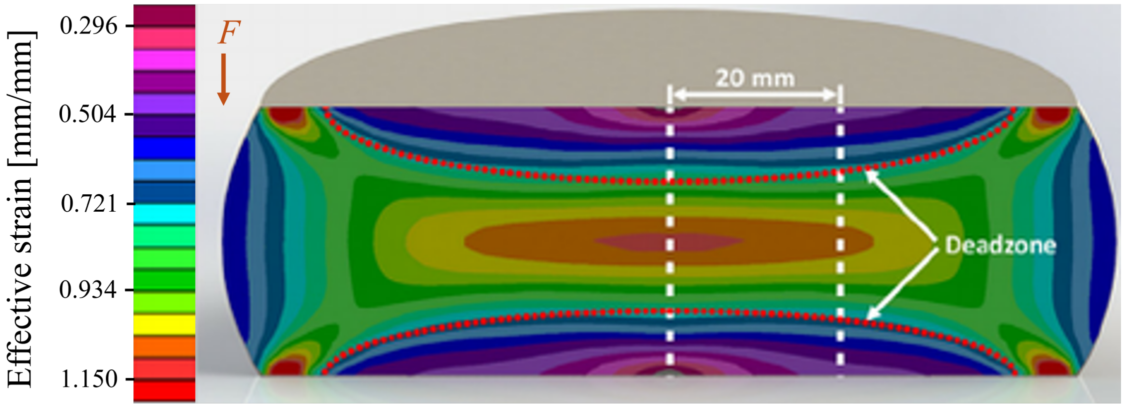

Figure 3.2: Example strain map of a forged Ni-based superalloy.

3.2 Defining the data

All data analysis was performed using Python. The development of all data processing functions was made using the dataset obtained at a temperature of 1100 °C, a strain rate of 0.05 s^{-1} and a strain of 0.3. Hence, all figures illustrated in Chapter 3 are of this dataset. The figures are collected at hold times ranging from 0 to 120 s, and the analysed hold time is at times shown in the plot title. Figure 3.3 shows examples of the obtained detector images, showing the green Debye-Scherrer rings.

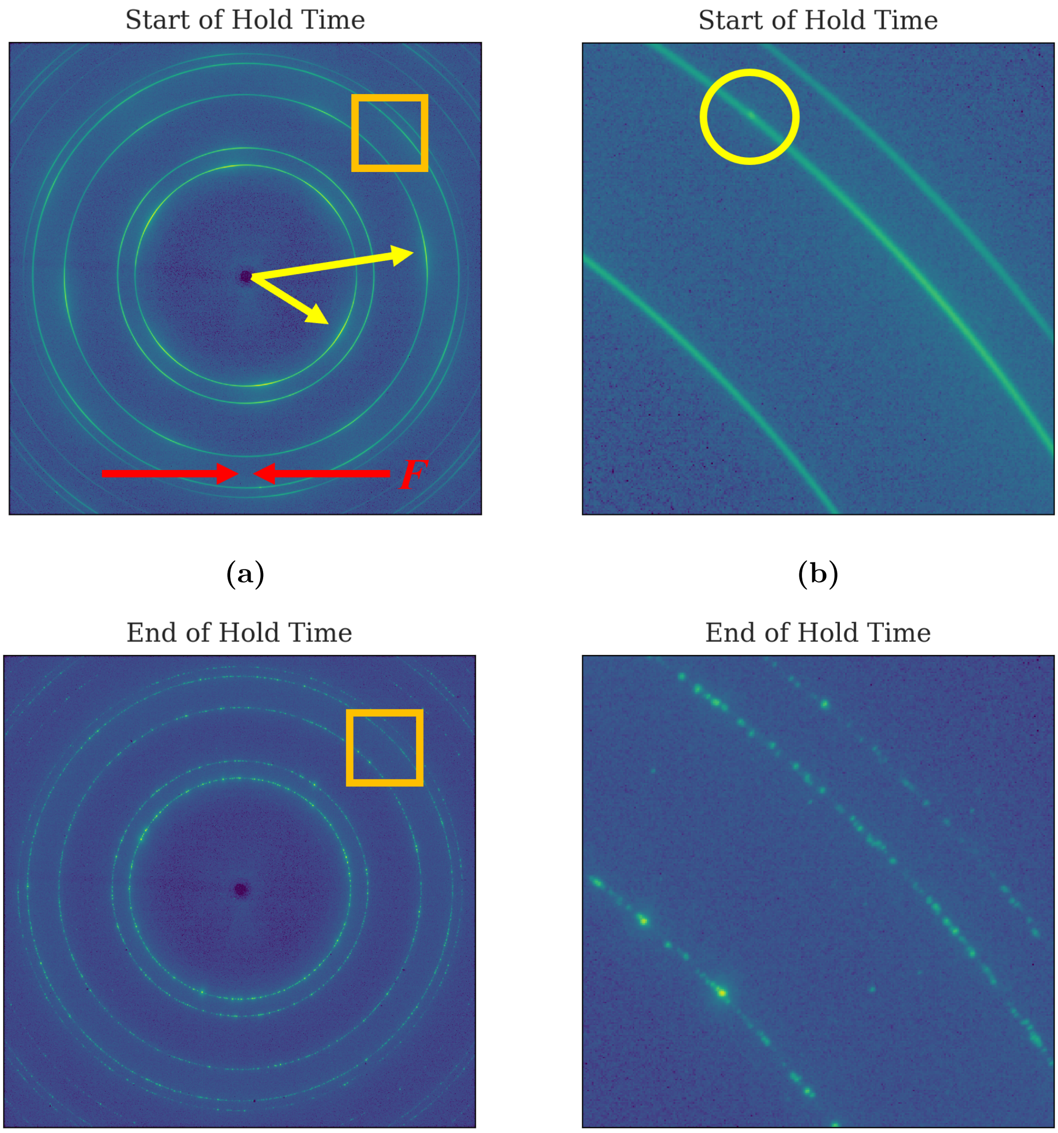

(a) **(b)**

(c) **(d)**

Figure 3.3: Resulting diffractograms after the deformation, at the start of the hold time in (a) and at the end of the hold time in (c). (b) and (d) show zoomed-in versions, with their respective areas illustrated by the orange square in the original images.

Figure 3.3a shows the XRD diffractogram right after the deformation, at the start of the hold time. The orange rectangle visible in this figure shows the location of the zoomed-in area of Figure 3.3b. Equivalently, Figures 3.3c and 3.3d show the final collected diffractograms — at the end of the hold time. The red arrows in Figure 3.3a indicate the direction of deformation of the sample in relation to the position of the detector. As seen, right after the deformation the intensity distributions around the Debye-Scherrer rings are smooth, illustrating the smeared out grains. Regions of higher intensity are further visible for each ring, showing the deformation texture. The yellow arrows in Figure 3.3a are directed towards a maximum in ring 111 and in ring 220 respectively, showing that the maxima appear at different χ. For the 111 ring, six maxima are visible. Discontinuous distributions are seen as the recrystallization has progressed, instead showing various high-intensity spots around the rings, representing the new grains formed. As marked by the yellow circle in Figure 3.3b it is visible that some recrystallized grains have nucleated already at the start of the hold time.

To process the tif-images, the Python libraries `PyFAI` and `fabio` were used [23] [24]. The intensity in the diffractograms is aimed to be separated into scattering from the sample (I_{sample}) and background (I_{bkg}). The background signal includes contributions from for example air scattering and incoherent Compton scattering from the sample. The sample signal is thereafter aimed to be separated into diffraction from deformed (I_{def}) and recrystallized (I_{RX}) grains, according to Equation (3.1).

$$I_{\text{tot}} = I_{\text{bkg}} + I_{\text{sample}} = I_{\text{bkg}} + I_{\text{def}} + I_{\text{RX}} \tag{3.1}$$

Initially, the 2θ-location of each ring had to be determined. This was done by integrating the whole image along the χ-axis. The results of this integration is shown in Figure 3.4, illustrating the intensity over 2θ at a hold time of 0 s, as well as the 2θ-locations of the first four rings.

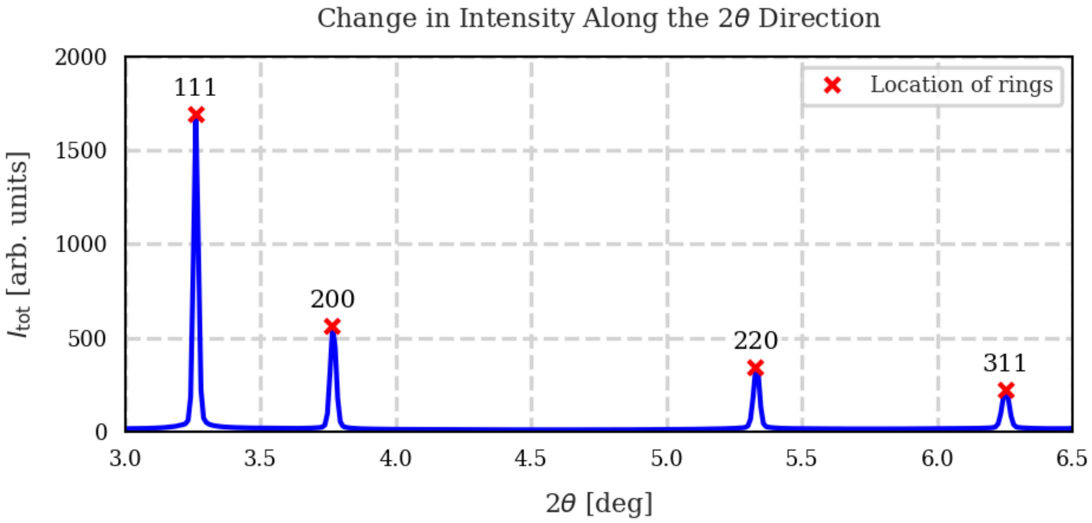

Figure 3.4: Result of the azimuthal integration, showing the 2θ-position of each ring.

To thereafter do the intensity analysis around an individual ring, the data was integrated in a 2θ-interval around the ring to get the average intensity of the whole ring width. This width was set to 0.3 degrees, chosen as it was narrow enough to not interfere with a neighbouring ring and wide enough to capture the width of a single ring. The effect of pixel resolution was then analysed, by looking at the pixel width of a single detected peak in the azimuthal direction. From this analysis, it was decided that each pixel should be split into 2.5 bins. The radius of each ring was then computed by $r_{hkl} = D\tan(2\theta_{hkl})$, where D is the distance from the sample to the detector and $2\theta_{hkl}$ the 2θ-location for a given ring. Computing the difference in radius of the outer and inner 2θ-boundaries coming from the 0.3 degree interval, gave a radial difference dr. This parameter was used to compute the number of bins in the radial direction as seen in Equation (3.2):

$$N^r_{hkl} = \mathrm{int}\left(\mathrm{split}\cdot\frac{dr}{px}\right), \tag{3.2}$$

where px is the pixel size. Similarly, the number of bins in the azimuthal direction was computed using the circumference of the ring as seen in Equation (3.3):

$$N^a_{hkl} = \mathrm{int}\left(\mathrm{split}\cdot\frac{2\pi r_{hkl}}{px}\right). \tag{3.3}$$

In this way, the angular resolution around each ring was kept constant. Using these computed parameters, the diffractograms could be integrated along the 2θ-direction to obtain the intensity distribution around a given ring. Figure 3.5 shows the diffractogram of ring 111 at different stages during the hold time. The χ-axis ranges from -180 to 180 degrees — i.e. around the whole ring, where 0 degrees is the direction of the deformation. Figure 3.5a shows the diffractogram at the start of the hold time. The six maximas resulting from the deformation texture are visible. After 2 seconds, recrystallized grains have appeared which is seen as the high intensity peaks on top of the deformed signal in Figure 3.5b. As the time progresses, the initially wide and tall deformed maximas shrink in size, as they are being replaced by the sharp recrystallized peaks. This is seen visually after 10 seconds in Figure 3.5c. At the end of the hold time in Figure 3.5d, the baseline of the signal becomes flat, as not much of the initially deformed regions remain.

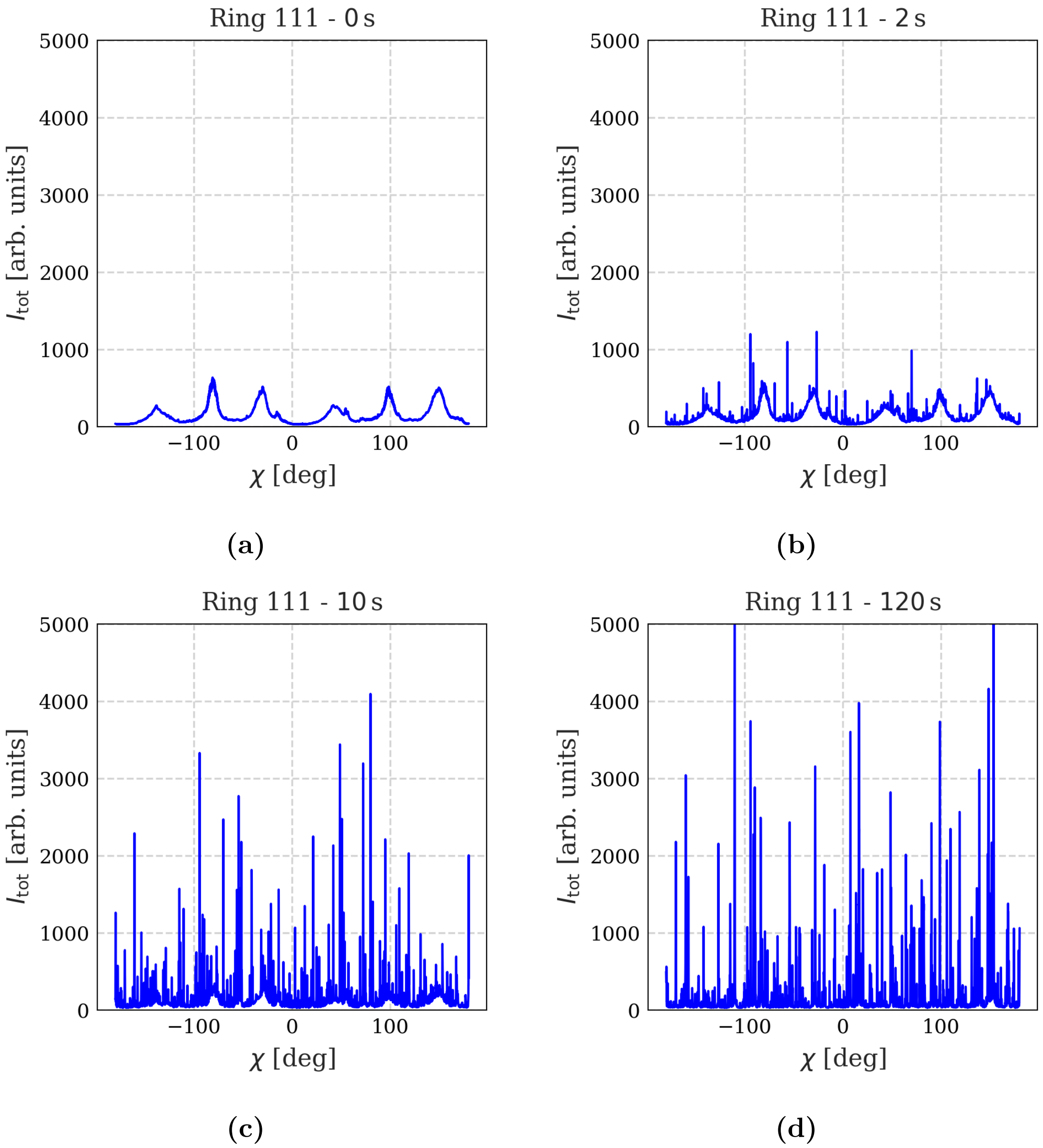

(a) **(b)** **(c)** **(d)**

Figure 3.5: Result of the 2θ-integration around the 111-ring, (a) at the start of the hold time, (b) after 2 s, (c) after 10 s and (d) at the end of the hold time at 120 s.

3.3 Background correction

The background intensity was then investigated. For this, the intensity along the 2θ-direction was examined, as this diffractogram showed a smooth signal with a clear base intensity, enabling a background signal to be extracted easily. Figure 3.6 shows the diffractogram for a limited intensity range, enabling the change in background intensity to be visualised. To make a fit to this background, the Python library `Pybaselines` was used [25]. This library provides algorithms to fit background signals to experimental data specifically. Various different algorithms were tried, and the method which provided the most accurate fit to the data was a Morphological and Mollified algorithm (mormol). This algorithm is based on mathematical morphology, which uses a set of transformations to provide a quantitative description to geometrical structures in data [26]. The morphological operation in the algorithm is combined with a mollifying kernel to smoothen the final fitted signal. The resulting background fitted to the azimuthal-integrated data is seen in Figure 3.6.

Note that as the background is extracted from integrating out the χ-dependence, it is assumed that the background is constant along the χ-axis. To verify this assumption, the maximum intensity difference in areas of mainly background signal was computed. The maximum intensity difference between pixels around a ring at half the 2θ-distance to ring 111 right after the deformation was found to be 5.11, and the maximum difference around a ring located between rings 200 and 220 was found to be 5.23. In comparison to the intensity variations of the whole diffractogram and specifically the intensities of individual peaks, these intensity difference were considered negligible, i.e. the background intensity could be assumed to be constant along the azimuthal direction.

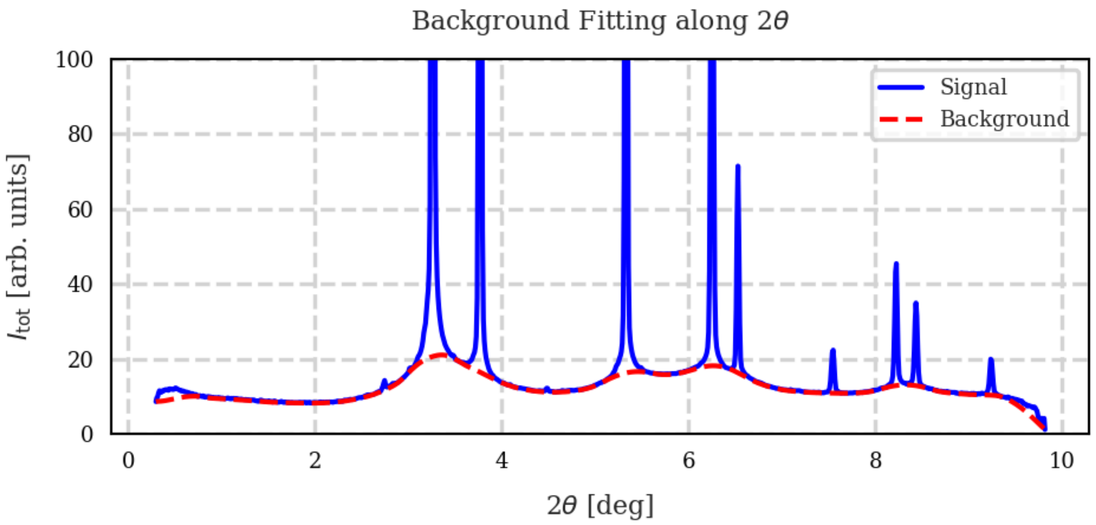

Figure 3.6: The intensity distribution along the 2θ-direction, together with the mormol background fit.

A three-dimensional representation of the entire background signal is seen in Figure 3.7, where the background intensity is seen to increase at the 2θ-value around each of the rings. Figure 3.8 shows three-dimensional plots of the intensity distributions around ring 111, where Figure 3.8a shows the full raw intensity distribution and Figure 3.8b the corresponding background fit.

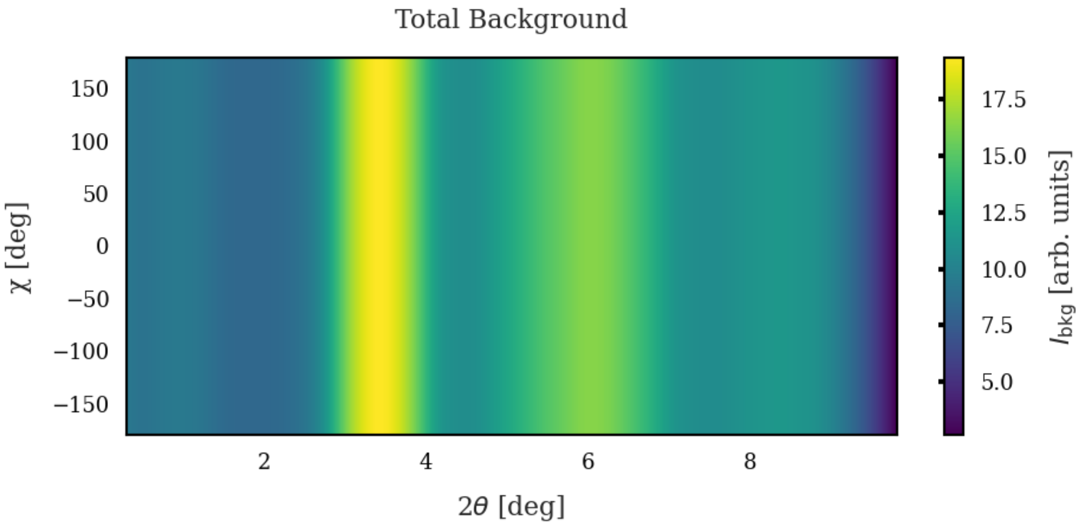

Figure 3.7: The total three-dimensional background map.

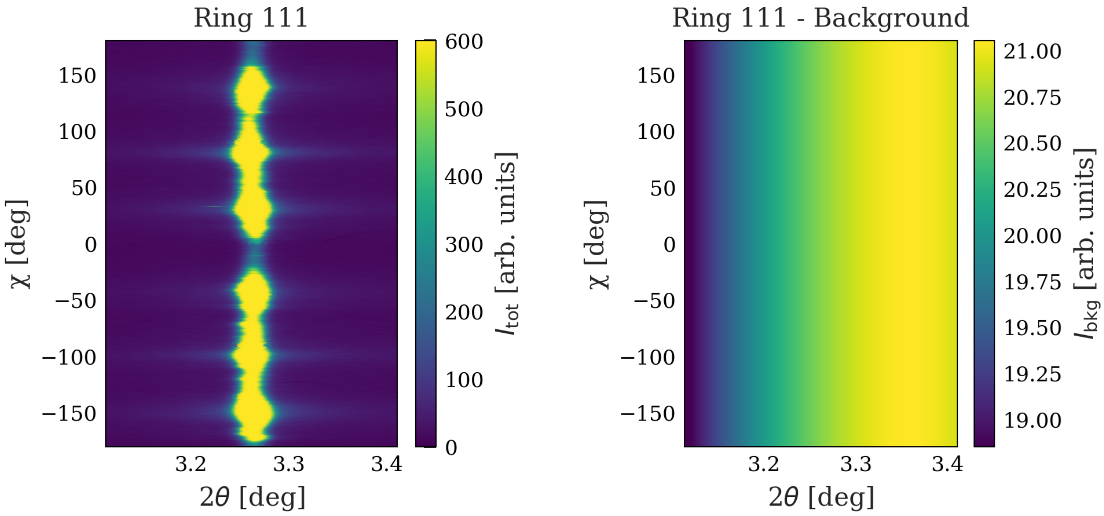

(a) **(b)**

Figure 3.8: Three-dimensional plot showing the intensity distributions along the 111-ring for a 2θ-interval around the ring: (a) shows the full intensity distribution and (b) the background intensities.

3.4 Extracting the deformed baseline

The data was thereafter integrated in the 2θ-direction. The part of the resulting diffractogram belonging to the diffraction from the deformed grains, named the baseline, was then aimed to be extracted. Initially, right after the deformation, most of the diffractogram consists of this baseline, as few recrystallized intensity peaks have been formed. Each ring initially consists of high intensity regions corresponding to the texture (preferred grain orientations) developed during deformation. The number and positions of the maxima for each ring depend on the crystal structure and deformation direction. For ring 111, these six regions are clearly visible, as seen in Figures 3.5a and 3.8a. To make a fit to this diffractogram, an individual distribution was fit to each region, and all distributions were then joined to a continuous curve. By this approach, information about the change in height and width of these regions, representing the change in deformation texture, could be obtained. Five different distributions were tested: Gaussian, Lorentz, Voigt, Pseudo-Voigt and Pearson VII. By comparing the absolute intensity difference between the data signal (I_{signal}) and the distribution fit intensity (I_{fit}) at each pixel value, the fractional intensity error (ϵ_{fit}) could be computed according to Equation (3.4).

$$\epsilon_{\text{fit}} = \frac{\sum |I_{\text{signal}} - I_{\text{fit}}|}{I_{\text{signal}}} \tag{3.4}$$

The computed errors are seen in Table 3.1, from which it is evident that using Lorentz distributions gave the most accurate fit to the data.

Table 3.1: Intensity error between the signal and fitted baseline

Distribution	ϵ_{fit}
Gaussian	24.97 %
Lorentz	13.10 %
Voigt	38.94 %
Pseudo-Voigt	25.00 %
Pearson VII	30.34 %

The Lorentz distributions follow the function defined in Equation (3.5):

$$f(\chi : \chi_0, I_0, \lambda) = \frac{I_0 \cdot \lambda^2}{(\chi - \chi_0)^2 + \lambda^2}, \tag{3.5}$$

where χ_0 and I_0 are the χ-position and maximum intensity of the peak, and λ the full width at half maximum (FWHM). The Lorentz distributions, and equivalently for the other distributions tried, were obtained using the functions *find peaks* and *curve fit* from the Python library `Scipy` [27]. Initially, the locations of the six peaks were obtained, from which the parameters needed for $f(\chi)$ were computed. The *curve fit* method was then used to fit the distribution to each peak individually. All peaks were then combined, and the final function was interpolated to ensure the resolution matched the data signal. The data signal together with the Lorentz fit is seen in Figure 3.9.

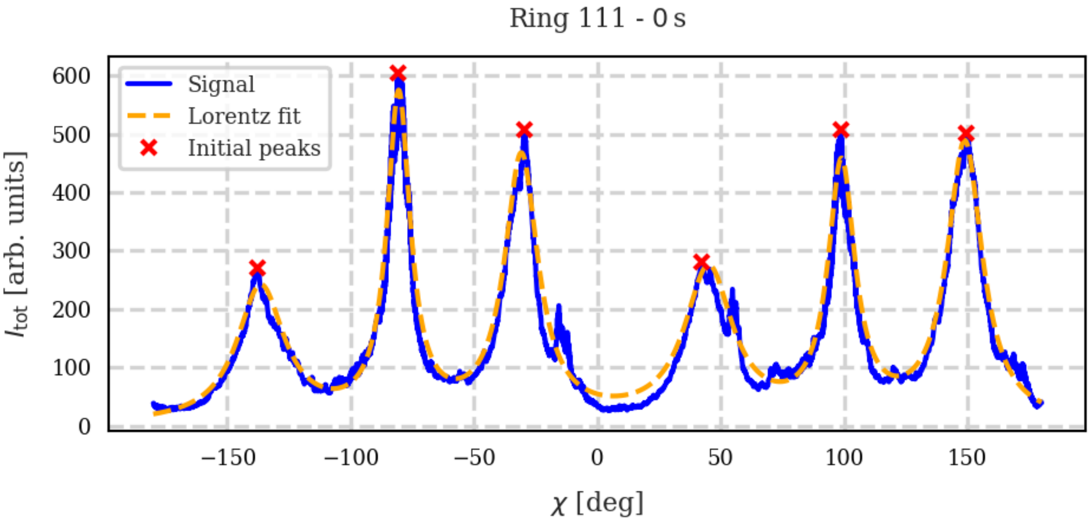

Figure 3.9: Intensity distribution around the 111-ring at 0 s, together with the combined plot of six Lorentz distributions.

After the distribution was found at 0 s, the distribution parameters extracted from the *curve fit* function were applied as a guess of the parameters at the next time step. A mask was also applied to the data, by only allowing the *curve fit* method to look for distributions within a given χ- and intensity interval. The χ-interval was set to go from and to half the distances to the neighbouring peaks, and the intensity interval to go up until twice the prior peak intensity. This part was vital for finding the distributions when the recrystallization became more evident in the form of new high intensity peaks on top of the deformed distributions. The explained method for finding the shape of the baseline worked well when the distributions had a well-defined height and width. As the recrystallized grains eventually replace the deformed ones, the deformed peaks start to decrease in size, and become more difficult to distinguish. The data signal together with the estimated Lorentz fit after 20 s is seen in Figure 3.10a. As visible, the baseline fit does not match the true baseline to the data. To solve this, a series of filters were applied. First, a minimum filter was applied to ensure that the baseline never exceeded the data signal. The results are shown in Figure 3.10b. To smoothen out the resulting noisy fit, a Gaussian filter was used. This filter modifies the data signal by a convolution with a Gaussian kernel, based on the Gaussian function as defined by Equation (3.6):

$$g(\chi) = \frac{1}{\sqrt{2\pi}\sigma} e^{-\chi^2/(2\sigma^2)}. \tag{3.6}$$

The standard deviation σ defines the kernel width, which controls how many neighbouring pixel data points are taken into account during smoothing. The standard deviation was set to 10, based on testing. The resulting baseline after the Gaussian smoothing is seen in Figure 3.10c. As the baseline still seemed to follow the data signal too much, giving a noisy signal, an additional smoothing method was applied. An excess intensity Δ was computed, by subtracting the data signal from the baseline. This yielded a negative Δ if the baseline was lower than the data signal and positive if greater. This value was then used to compute a sigmoid-based suppression, as described in Equation (3.7):

$$\text{suppression} = \Delta \cdot \frac{1}{1 + e^{\alpha \Delta}}, \tag{3.7}$$

where the parameter α helped control the level of suppression and was set to 10 after testing. The suppression parameter was then subtracted from the baseline, increasing its value if it was initially underestimated and decreasing its value if overestimated. The use of the sigmoid function helped to maintain the smooth baseline signal while moving it closer towards the data signal. After subtracting the suppression, the Gaussian smoothing filter was applied again. This method was repeated five iterations for better convergence towards the true baseline. At the end, the minimum filter was applied again, to ensure that the final baseline stayed below the data signal. The result is shown in Figure 3.10d.

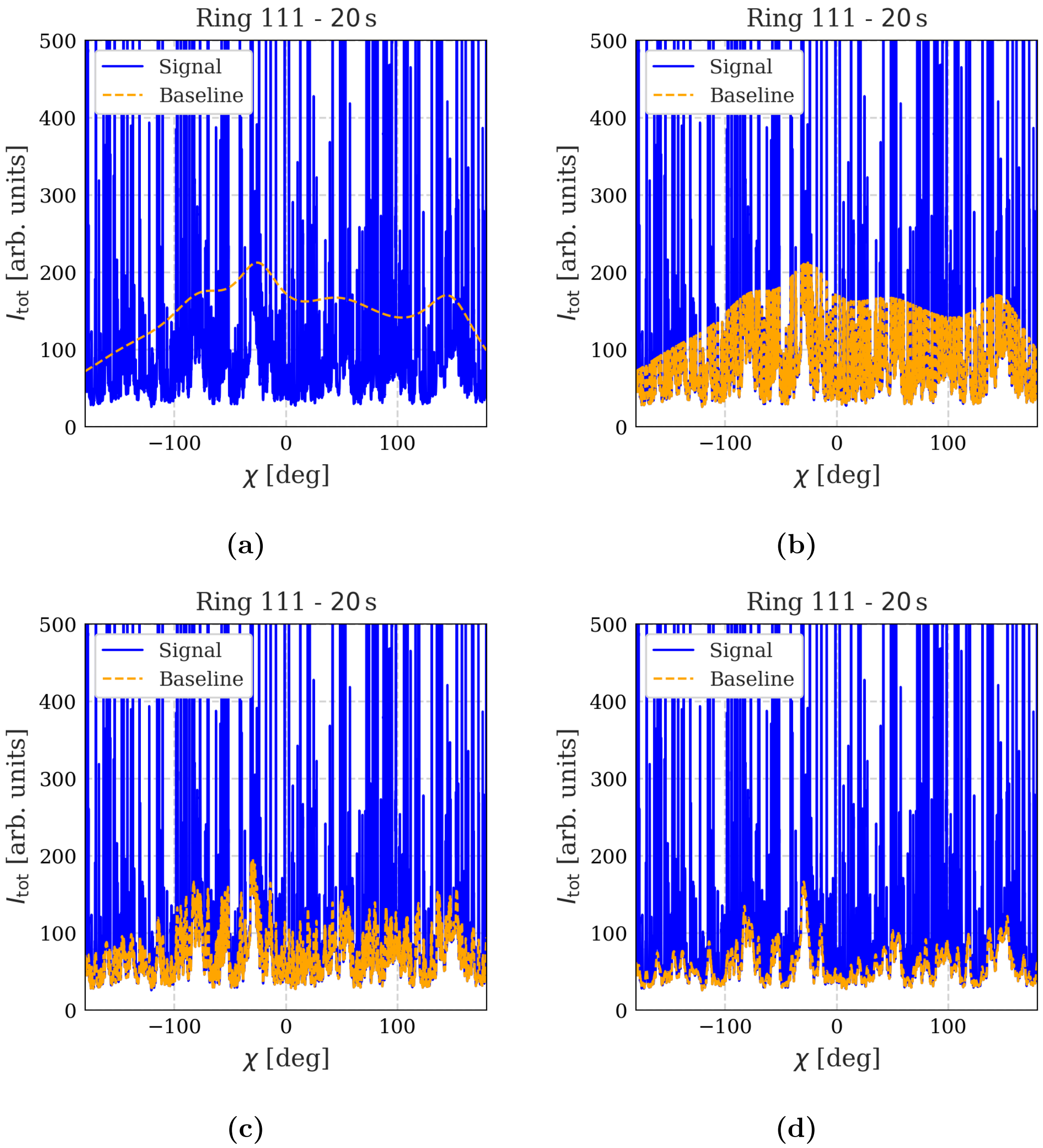

(a)

(b)

(c)

(d)

Figure 3.10: The baseline estimation at 20 s: (a) using a Lorentz distribution fit, (b) added constraint that the baseline never exceeds the data signal, (c) applying a gaussian filter and (d) after using the Sigmoid suppression.

After around 20 s, the distributions became too small to be distinguishable. An alternative method was then developed. Starting at the minimum value of the χ-axis, the minimum intensity value within a set χ-range was saved as described in Equation (3.8):

$$\min\left(I_{\text{signal}}(\chi_i), I_{\text{signal}}(\chi_{i+\text{steps}})\right), \tag{3.8}$$

where $i \in [0, N^a_{hkl} - \text{steps}]$ and i increments by steps. The saved minima were concatenated and interpolated to get the same resolution as the data signal. The effect of the chosen step parameter was investigated, by visually examining how the computed baseline followed the data. The steps was set to 40 bins. The N^a_{hkl} for ring 111 was calculated to 7539 from Equation (3.3), meaning that 189 minimum values were used for creating the baseline. The data signal together with the step baseline method at 5 s is seen in Figure 3.11. Figure 3.11a shows the diffractogram of the whole χ-range, and Figure 3.11b shows a zoomed-in version where both the distribution and step methods are visible.

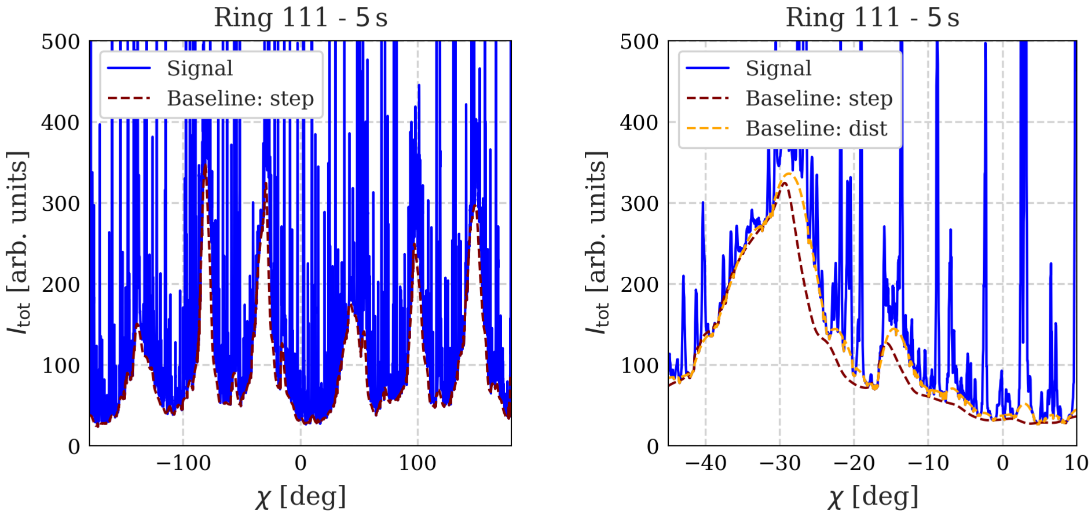

(a) **(b)**

Figure 3.11: Baseline estimation at 5 s, (a) using the step method, and (b) using both the step and distribution method.

As can be seen, the step method underestimates the true baseline at the large deformed regions due to the large step size chosen, but works well for the flatter regions, where the distribution method instead follows more of the noise. One way of addressing this could be to change the step size dynamically at the different regions at different time steps. An alternative method is to work with both the distribution and step methods simultaneously. The latter approach was chosen. First, when the deformed regions were large in size, the distribution method was used alone. When more flat regions started to form, a weighted average was computed between the two methods as defined in Equation (3.9), where dist and step denote the respective methods. This average was used between the time t_{start} and t_{finish}. The weight $w(t)$ was dynamically changed in a continuos manner over this time period, such that the transition between the methods was smooth. After t_{finish}, the step method was used alone as the distributions became indistinguishable. The times t_{start} and t_{finish} were set separately for each ring, by visually examining the evolution of the true baseline.

$$w(t)\cdot \text{dist} + (1-w(t))\cdot \text{step}, \quad \text{with} \quad w(t) = \begin{cases} 1, & t \leq t_{\text{start}} \\ \dfrac{t_{\text{finish}} - t}{t_{\text{finish}} - t_{\text{start}}}, & t_{\text{start}} < t < t_{\text{finish}} \\ 0, & t \geq t_{\text{finish}} \end{cases} \tag{3.9}$$

Note that there is still a risk that the baseline follows the lowest intensity points too well, potentially leading to an overestimation of fluctuations in the data. In cases where multiple peaks overlap, it might appear as if the baseline increases, but this effect might actually by due to the superposition of peaks rather than a true baseline shift. It is therefore important to keep in mind that while the computed baseline may visually follow the expected trend, its absolute value may still be inaccurate.

3.5 Recrystallized fraction

When the background and baseline methods had been developed, the total signal could be split into the three contributions I_{bkg}, I_{def} and I_{RX}. The areas between these signals are shown in Figure 3.12, where 3.12a shows the diffractogram after 2 s, and 3.12b after 5 s. The background area (A_{bkg}) is seen in red, the deformed baseline (A_{def}) in yellow, and the recrystallized area (A_{RX}) in blue. By separating these areas, the total f_{RX} could be computed according to Equation (3.10).

$$f_{\mathrm{RX}} = \frac{A_{\mathrm{RX}}}{A_{\mathrm{RX}} + A_{\mathrm{def}}} \tag{3.10}$$

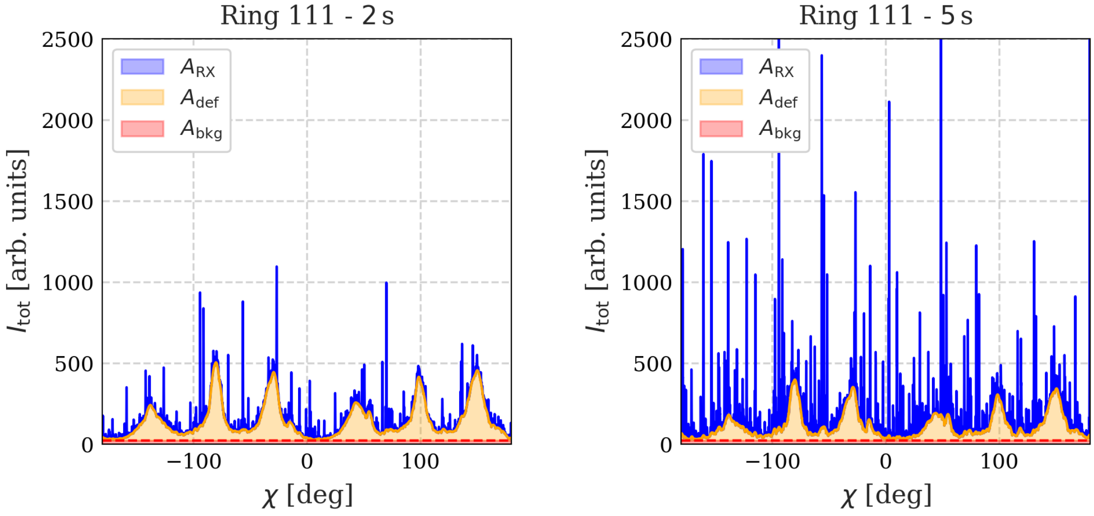

(a) **(b)**

Figure 3.12: Intensity distribution around ring 111, (a) after 2 s and (b) after 5 s. The separation of the signal into the three intensity areas are shown.

3.6 Change in grains over time

The change in f_{RX} describes how the fraction of recrystallized grains evolve. To get a more detailed understanding of this process, the number of peaks, corresponding to the number of grains, can be studied. The intensity of a peak increases with the size of the grain from which it is diffracted [17]. Studying how the intensity of the peaks evolve over time will thereby give an indication of the growth of the grains in the sample. For finding peaks, the background and baseline were subtracted from the data signal. To locate the peaks in the diffractograms, the function *find peaks* from `Scipy` was used. This function finds all local maxima in the data, thereby also counting noise or simple fluctuations as peaks. To only capture the considered real peaks, three filtering methods were used. First, a constraint was set on the minimum absolute intensity of a peak. The number of peaks detected for five different minimum intensities is seen in Figure 3.13. As seen in Figure 3.13a, the curves follow the same shape, but differ in magnitude. That is, the number of new found peaks and the new detected numerical noise within the new intensity interval seem to be constant.

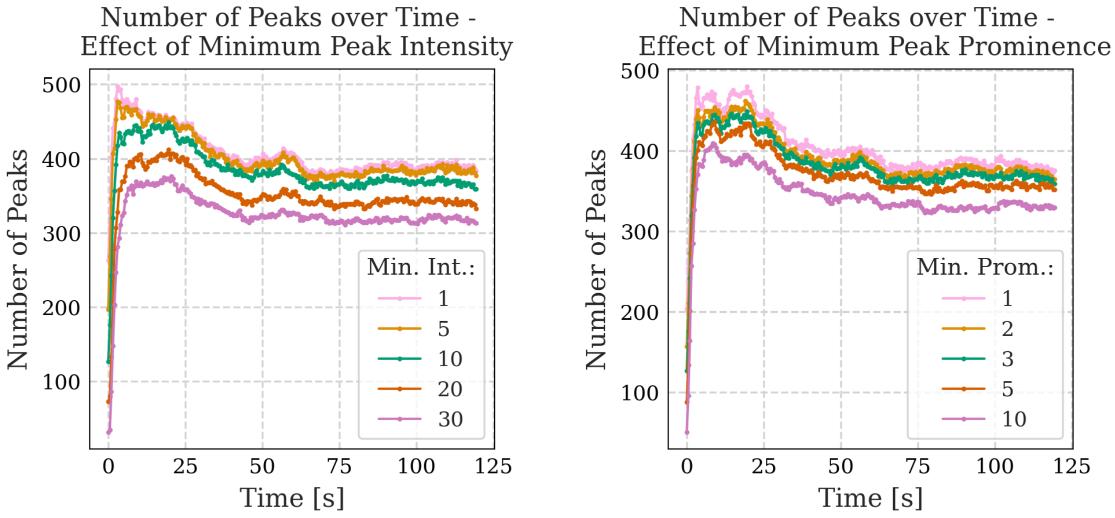

(a) **(b)**

Figure 3.13: The number of detected peaks over time, (a) for different cut-offs of minimum intensities and (b) of minimum peak prominences. In (a) the minimum peak prominence is set to 3, and in (b) the minimum peak intensity is set to 10, such that the green curves in the plots are the same.

The low intensity peaks close to the different cut-off intensities were then examined visually in the diffractograms. Figure 3.14 shows the diffractogram of ring 111 at 50 s for a limited χ-range. Figure 3.14a shows the range for the full intensity interval, showing both larger and smaller peaks. Figure 3.14b shows the same diffractogram but for a limited intensity interval. In both figures, a threshold minimum intensity of 10 is set for the detected peaks. As visible from Figure 3.14b, several well defined peaks are present right above the threshold.

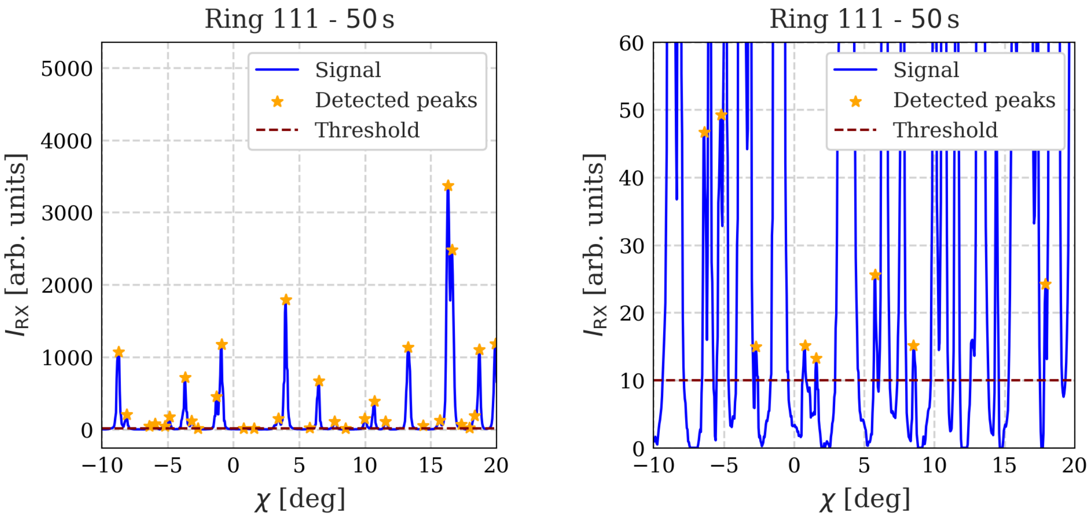

(a) **(b)**

Figure 3.14: Intensity distribution around ring 111 at 50 s, showing the detected peaks above a threshold minimum intensity of 10.

As visible in Figure 3.13a, there also exists peaks below the threshold intensity of 10. Two of these peaks can be seen in Figure 3.15, marked with red crosses. It might be difficult to understand which of such small peaks are a result of diffraction from small grains, and which are fluctuations in the data. As the baseline has been subtracted from the data signal, any fluctuations in this baseline can have resulted in false peaks, which is why it is important for the baseline to be a smooth function. The threshold of 10 was decided to be sufficient to capture the actual peaks, and to avoid small fluctuations in the data counting as peaks.

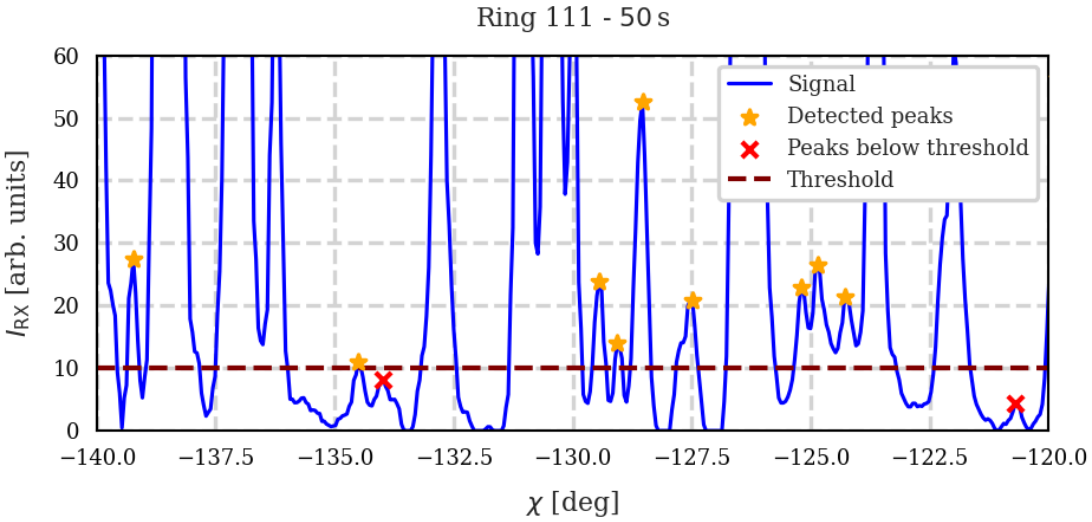

Figure 3.15: Intensity distribution around ring 111 at 50 s, showing peaks located above and below the set threshold minimum intensity of 10.

The second constraint was set on the prominence of a peak. Smaller fluctuations in the data located on the shoulder of a large principal peak can have a large absolute intensity while not being an actual peak. The effect of minimum peak prominence on the number of detected peaks is shown in Figure 3.13b. Again, the curves of minimum prominence follow the same shape but differ slightly in magnitude. By visually examining the intensities of small peaks at different time instances, the minimum prominence was set to 3.

Lastly, a constraint was set on the minimum distance between two neighbouring peaks. In the case that a single data point on a peak has lower intensity than the two neighbouring data points, a single actual peak can appear as two. Figure 3.16a shows the effect of minimum peak distance in bins on the the number of detected peaks. This constraint does not affect the results remarkably for small distances, as the total number of peaks are great in magnitude compared to the rare case of these false peaks. The minimum number of bins between peaks was set to 3. If two peaks are found within this minimum distance, the peak of highest prominence is kept. Figure 3.16 shows an example of three smaller peaks located close to each other (the same peaks are also visible in Figure 3.15). The peaks are well defined in intensity, prominence and distance between each other.

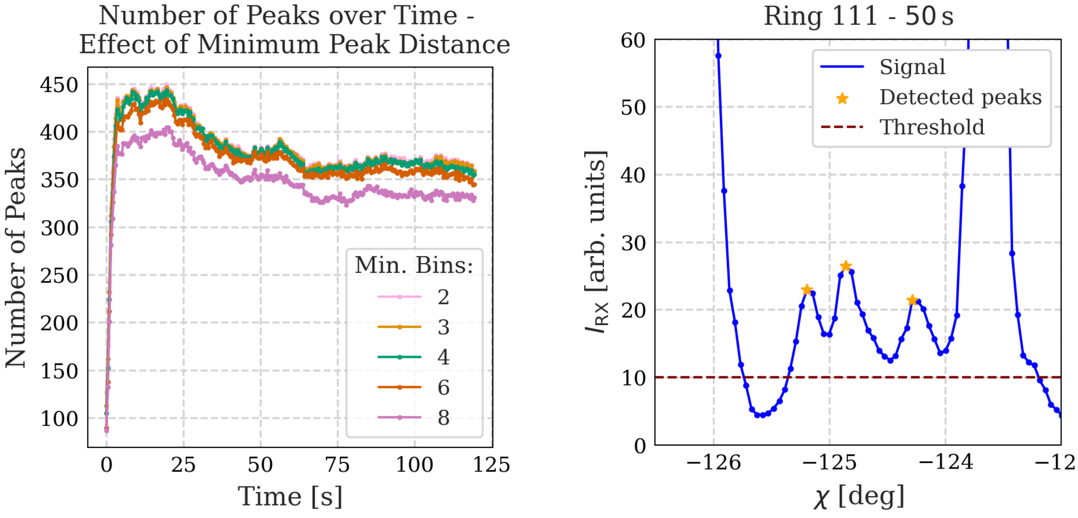

(a) (b)

Figure 3.16: Figure showing the effect of minimum peak distance on the number of detected peaks in (a), and (b) shows an example of three small well defined peaks located close to each other.

4

Results and Discussion

This chapter covers and discusses the computed results. First, the results of the created functions are presented, and a comparison is made between datasets of different deformation temperatures. Thereafter, these results coming from XRD data are compared to the EBSD results from Eriksson et al. [5].

4.1 Recrystallized fraction

Figure 4.1 shows the computed f_{RX} over time. Figure 4.1a shows the values for ring 111 specifically, where the f_{RX} is shown to start at around 4 %, then increasing rapidly before starting to converge after around 20 s and reaching a f_{RX} of around 90 % at 120 s. The f_{RX} over time for all rings is seen in Figure 4.1b, showing curves that converge at slightly different speeds but that follow the same shapes and reach similar final values.

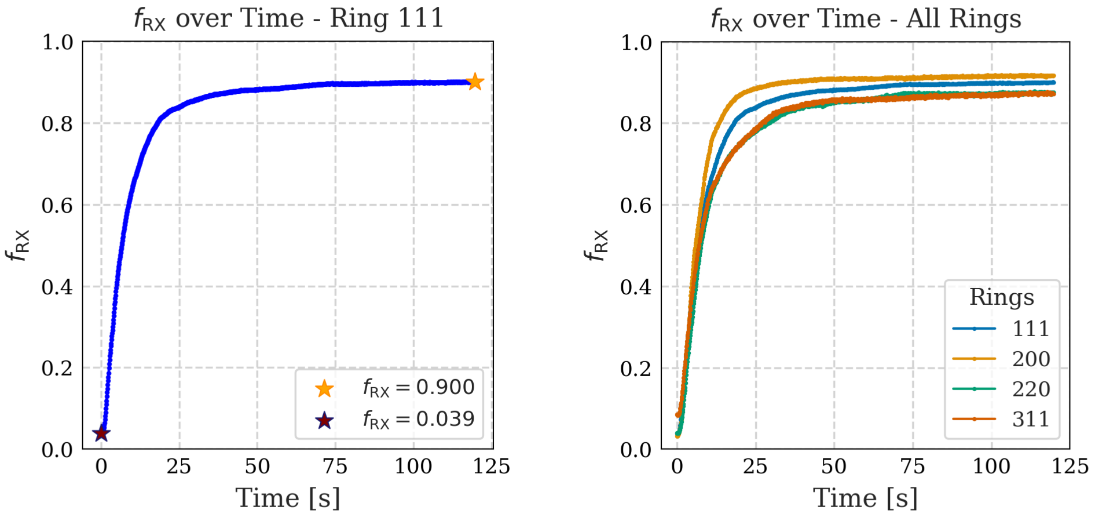

(a)

(b)

Figure 4.1: Change in f_{RX} between 0 and 120 s, (a) for ring 111 illustrating the initial and final values of around 4 % and 90 %, and (b) for all rings.

The deformed grain density obtained from different rings might vary, due to the preferred orientation of the grains in the deformed material, which might explain why the recrystallization is not identical when comparing the results from different rings. Another thing to consider would be if the different preferred orientations have different dislocation densities throughout the sample. The strain, and hence the dislocation density, varies in the volume studied, and is typically greater at the centre of the sample as discussed from Figure 3.2. If one texture component is more common at the outer regions of the sample, where the amount of dislocations is lower, this part may recrystallize slower.

4.2 Nucleation and growth of recrystallized grains

Figure 4.2 shows the change in number of detected peaks over time. Figure 4.2a shows the peaks around ring 111, starting at 127 detected peaks, then increasing rapidly before reaching a maximum of 453 peaks at 19 s. The number then decreases and converges towards a number of 356 peaks at 120 s. The change in number of peaks gives information about the mechanisms of the recrystallization. The increase in number of peaks suggests that new grains nucleate at the start of the hold time. The decrease then suggests that the recrystallized grains begin to grow at the expense of other grains.

Figure 4.2b shows the change in number of peaks for all rings. Again, the absolute values of the different rings differ but the curves follow the same shape. The number of peaks in 311 is noticeably higher compared to the other rings. One explanation to this could be that the set of 311 planes has the highest multiplicity of 24 out of the sets studied. Similarly, ring 200 with the lowest number of peaks is the set of lowest multiplicity of six.

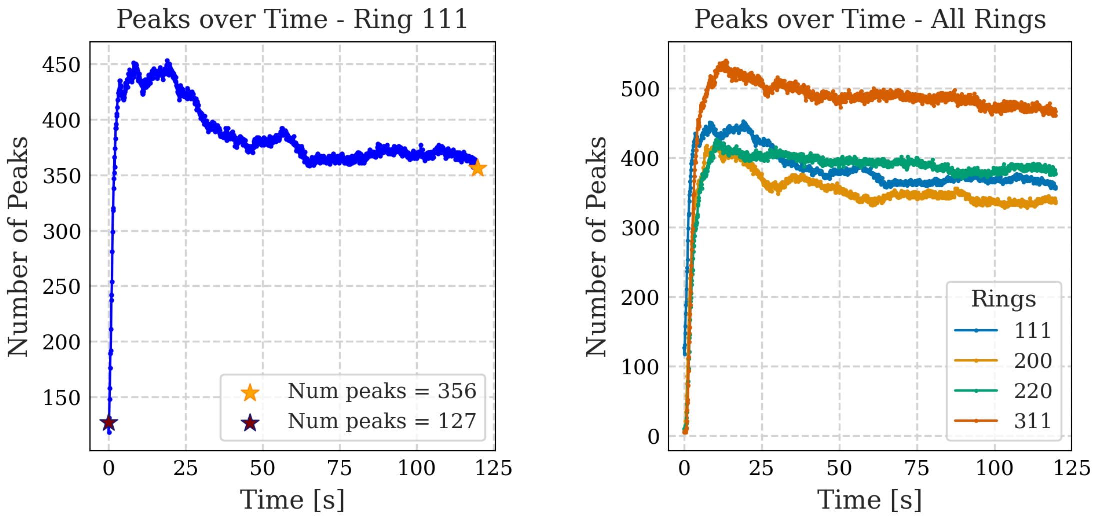

(a) (b)

Figure 4.2: Change in number of peaks between 0 and 120 s, (a) for ring 111 illustrating the initial and final numbers of 127 and 356 peaks, and (b) for all rings.

The intensities of the detected peaks were then studied, to get an understanding of how the grains changed in size during the hold time. First, single peaks were tracked over time. Figure 4.3 shows an example of the progression of a single peak over time. This peak started to emerge after around 0.5 s, and then quickly increased in intensity. The maximum intensity of this peak was reached after around 5 s, and from that time onwards the peak maintained a similar intensity. The fast growth of the peak is a demonstration of the fast increment of the f_{RX}, as the newly created grain grew to replace the initially deformed grains.

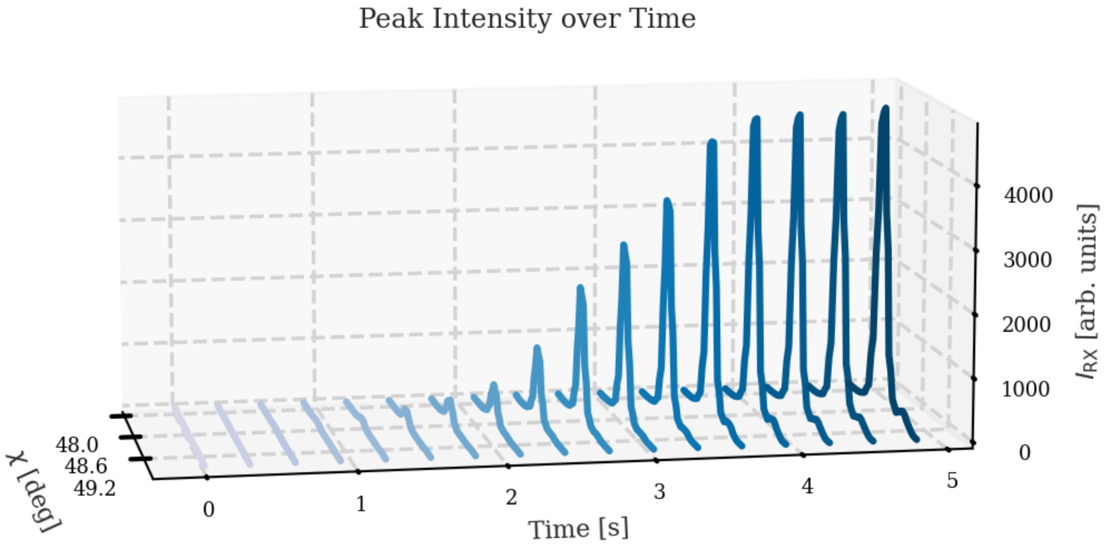

Figure 4.3: Change in shape of a single peak over time.

The average intensities of all detected peaks for each ring is illustrated in Figure 4.4. The grains are seen to grow in size on average, but do converge, especially for the rings 200, 220 and 311. The convergence of both the number and size of recrystallized grains support the observed stabilization of the f_{RX} in Figure 4.1b. Note that the intensities of peaks cannot be directly compared between the rings, as the intensity of a peak is controlled by the structure factor which decreases with increasing Miller indices. The intensity of peaks can also get attenuated due to thermal motion as described by the Debye–Waller factor, and this attenuation increases with increasing Miller indices [28].

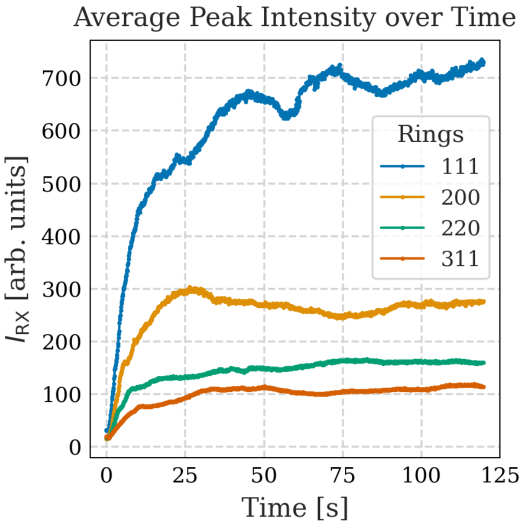

Figure 4.4: Change in average intensity of the detected peaks around all rings.

To get a better understanding of the spread in the distribution of grain sizes, histograms of the peak intensity distribution at each time step were created. A kernel density estimation (KDE) was fitted to the histograms to get a smooth probability density estimation for each distribution. Figure 4.5 shows a mesh plot of the KDE over time between 0 and 5 s, where the peak intensity is plotted in log-scale. Note that the scale of the probability density colouring is shifted to better illustrate the small changes. Initially, at 0 s, there is a great probability density for peaks of low intensity, meaning small grain size. The probability density is further zero for intensities greater than 100. As time progresses, the grains increase in size, which is seen visually as a spread in density towards higher intensities. After 5 s the grain size distribution becomes much wider, which is seen by a lower and more even density distribution.

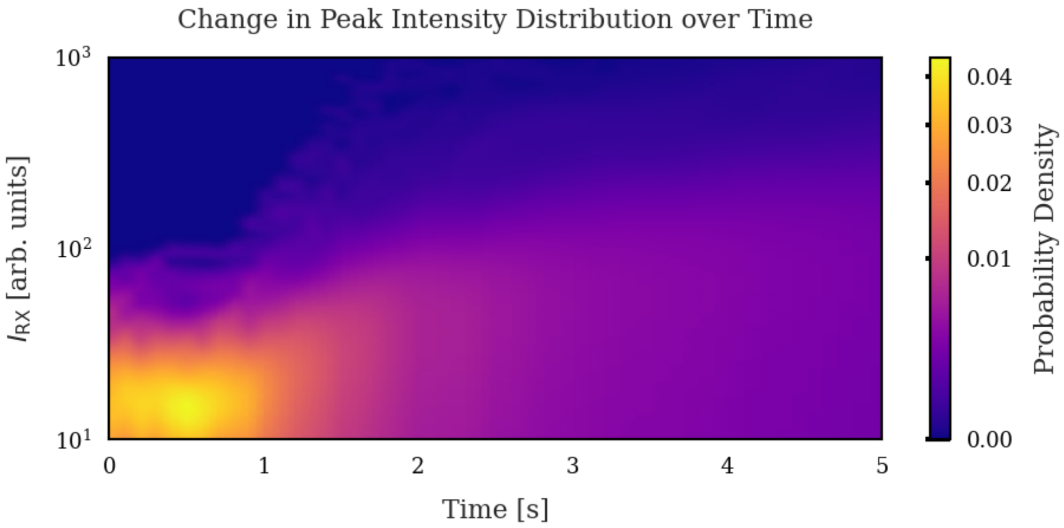

Figure 4.5: Change in the distribution of peak intensities for ring 111 over time.

4.3 Temperature dependence

The methods for computing f_{RX} and detecting peaks were applied to two additional datasets, each from using the same strain of 0.3 and strain rate of 0.05 s^{-1} but for 20 °C higher and lower temperature than the initial dataset (i.e. 1120 °C and 1080 °C). Figure 4.6 shows the change in f_{RX} over time for the dataset of 1120 °C. Figure 4.6a shows the values for ring 111, starting at around 4 % and ending at around 94 % after 120 s. Figure 4.6b shows the curves for all rings, here showing very similar shapes and values. Figure 4.7 shows the change in f_{RX} for the dataset of 1080 °C. Figure 4.7a shows a starting fraction of around 13 % and a fraction of around 80 % after 120 s for ring 111. The rate of change is less rapid for this dataset, and the starting point of convergence appears much later. This behaviour is followed for all rings in the diffractogram, as shown in Figure 4.7b. The f_{RX} results for all rings in each dataset are very similar, suggesting that the recrystallization is fairly homogenous for grains of different orientation.

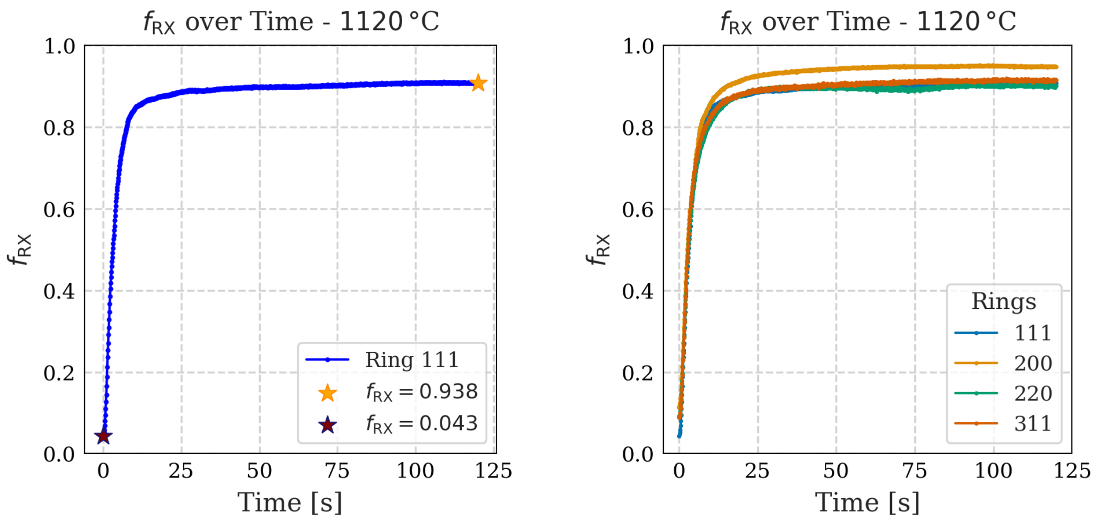

(a) **(b)**

Figure 4.6: f_{RX} over time for dataset of 1120 °C, (a) for ring 111 showing an initial value of around 4 %, and final value of around 94 %, and (b) for all rings.

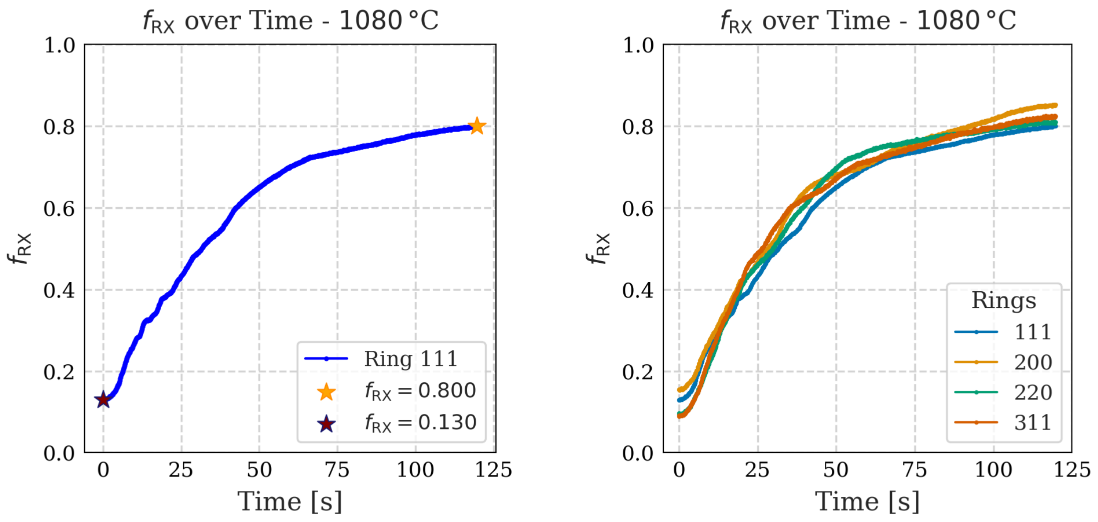

(a) **(b)**

Figure 4.7: f_{RX} over time for dataset of 1080 °C, (a) for ring 111 showing an initial value of around 13 % and final value of around 80 %, and (b) for all rings.

Figure 4.8 shows the average f_{RX} over all rings, for each of the three datasets over time. The fractions at 0 and 120 s hold time are listed in Table 4.1. In general, an increase in deformation temperature increases the recrystallization kinetics, which has been experimentally shown for Ni-based superalloys previously [8][29]. The influence of temperature on the rate of nucleation and growth of recrystallized grains has been described to follow an Arrhenius-type relationship, suggesting an exponential dependence [13]. This can explain the slower rate of recrystallization for the dataset of 1080 °C.

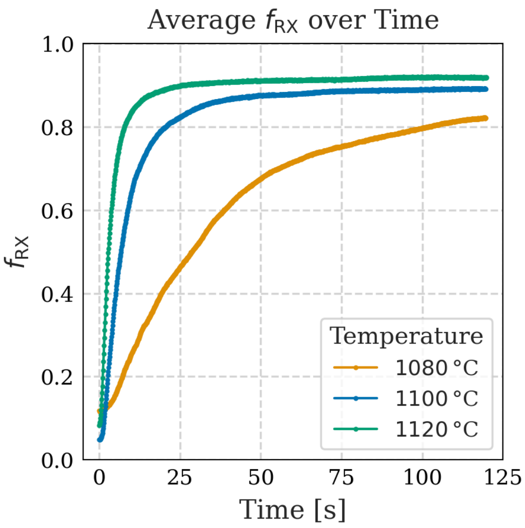

Figure 4.8: Average f_{RX} for different datasets over time. The average is taken from all rings in each dataset, showing how the temperature affects the rate of recrystallization.

It is important to note that the average plane-wise f_{RX} may not be a fully representative measure of the total recrystallized fraction in the sample. After the deformation, some orientations may dominate as described by the texture, while other orientations might be more rare. Assigning equal weight to all rings when calculating the average f_{RX} could therefore lead to a misleading estimation of the total fraction. On the other hand, as the fractions in the individual rings had similar shapes and magnitudes, as seen in Figures 4.1b, 4.6b and 4.7b, the impact on the average value may be limited. However, for a more accurate analysis, future work could incorporate the initial texture distribution to weight the contribution from each orientation accurately. In addition, it is important to note that the results for a certain temperature come from a single sample. Sample specific variations, or slightly different alignment of the beam for each sample may have influenced the results. This might for example explain why the recrystallized fraction starts at a higher value for the 1080 °C dataset, as seen in Table 4.1. For better statistics, multiple samples can be tested for each temperature.

Table 4.1: Initial and final average f_{RX} for each dataset

Temperature [°C]	f_{RX} 0 s	f_{RX} 120 s
1080	12 %	82 %
1100	5 %	89 %
1120	8 %	92 %

Figure 4.9 shows the change in number of peaks over time, in Figure 4.9a for the dataset of 1080 °C and in Figure 4.9b of 1120 °C. The greater value of number of peaks in ring 311 is again visible for both datasets. The initial increase in number of peaks for both datasets suggests that recrystallized grains nucleate, and it is visible that greater deformation temperature leads to faster nucleation. The decrease in peaks in the dataset of 1120 °C further suggests that the growth of grains, at the expense of other grains, start to dominate any nucleation of new grains. This trend is not as clear for dataset of 1080 °C.

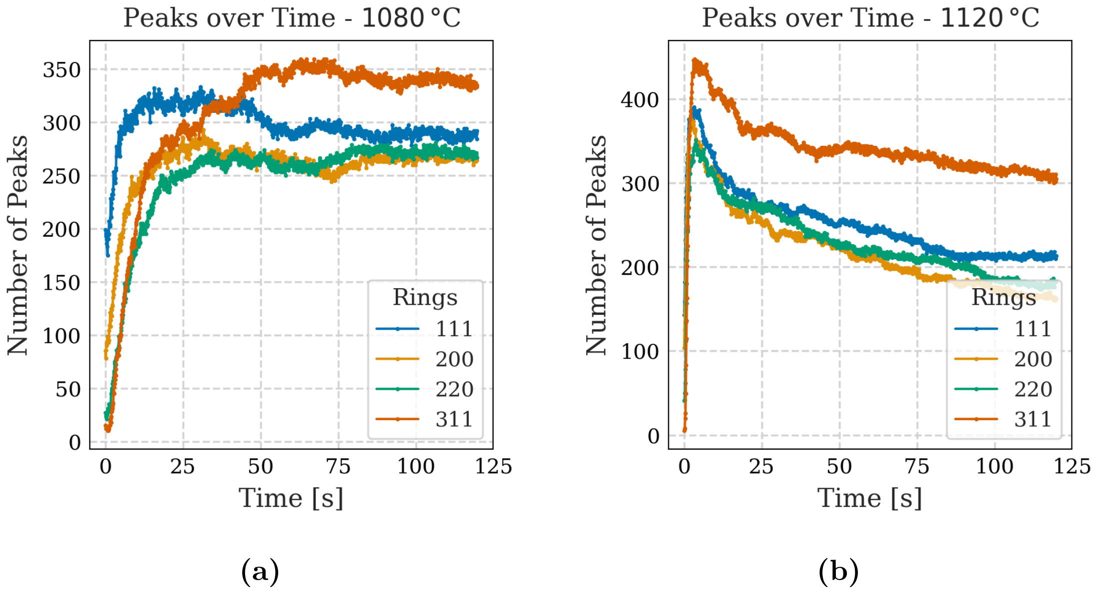

Figure 4.9: Change in number of detected peaks for each ring, (a) in the dataset of 1080 °C and (b) of 1120 °C.

Figures 4.10, 4.11 and 4.12 show the total number of peaks from all rings together with the average f_{RX} over time for each dataset respectively. From these figures it is visible that faster nucleation of grains leads to faster convergence of the total recrystallization. It is also visible that a faster rate of nucleation is followed by a faster reduction of grains, as a result of grain growth.

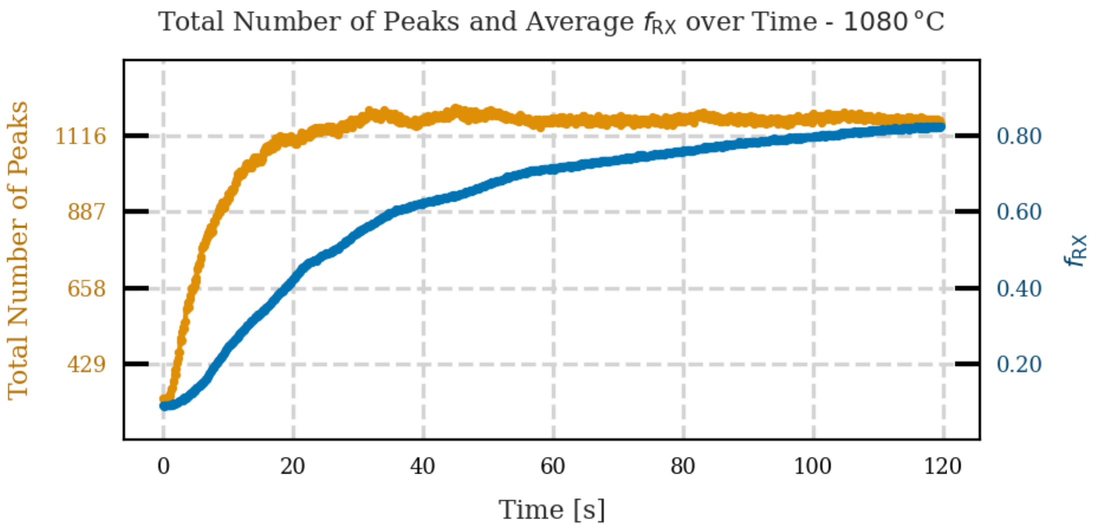

Figure 4.10: Change in total number of peaks from all rings, together with the average f_{RX} over time for the dataset of 1080 °C.

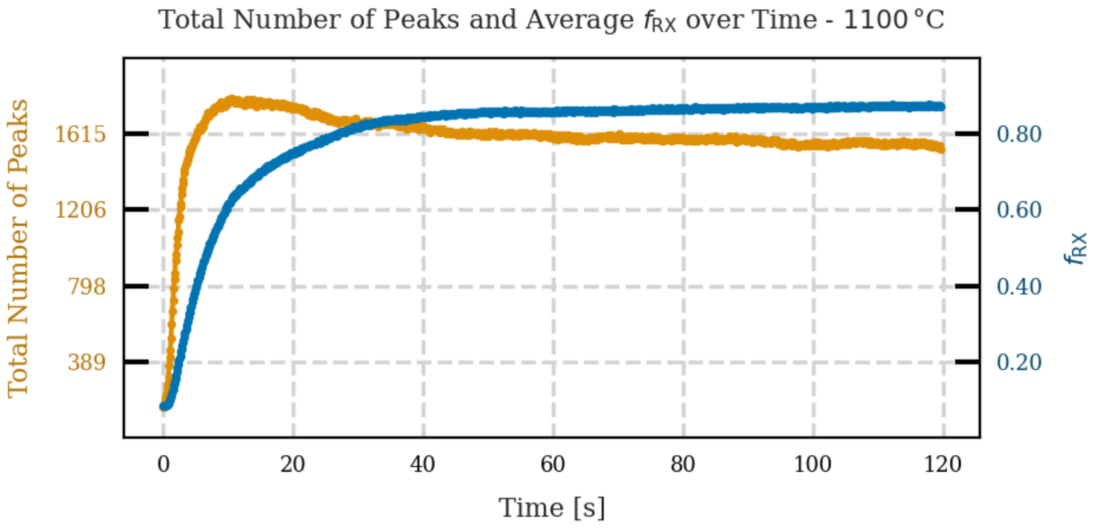

Figure 4.11: Change in total number of peaks from all rings, together with the average f_{RX} over time for the dataset of 1100 °C.

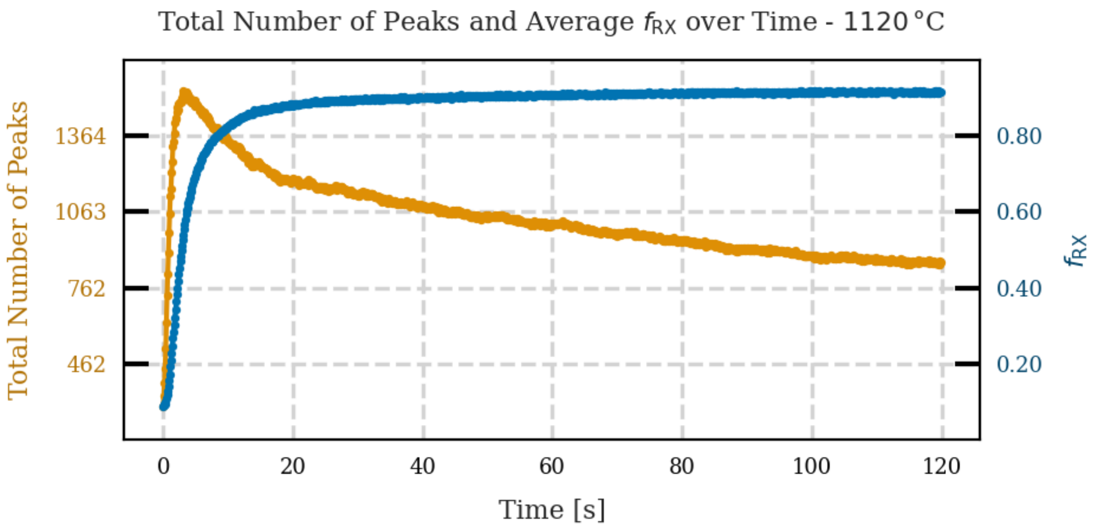

Figure 4.12: Change in total number of peaks from all rings, together with the average f_{RX} over time for the dataset of 1120 °C.

Figure 4.13 shows the average intensity of the detected peaks over time, in Figure 4.13a for the dataset of 1080 °C and in Figure 4.13b of 1120 °C.

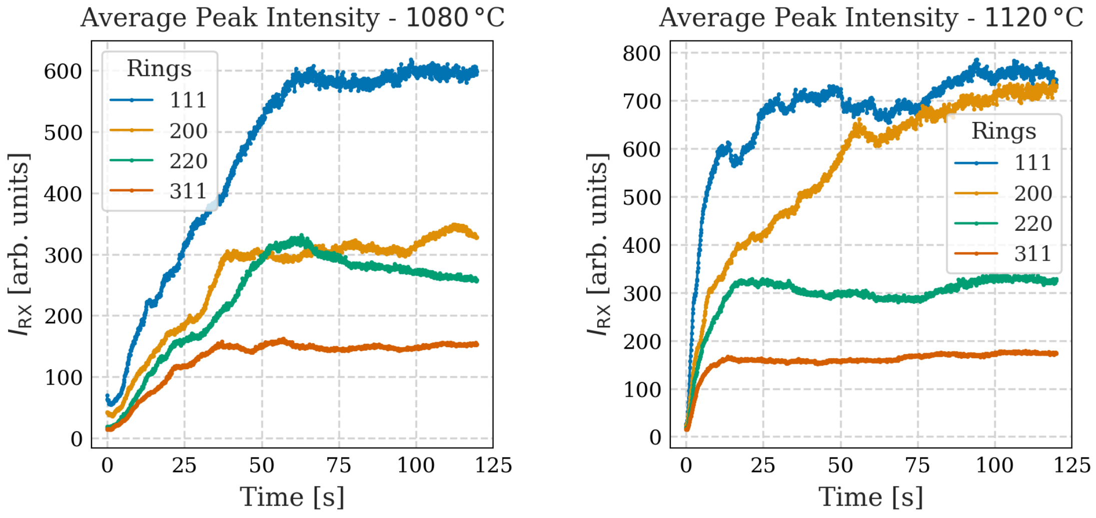

(a) **(b)**

Figure 4.13: Change in average intensity of the detected peaks, (a) in the dataset of 1080 °C and (b) of 1120 °C.

Figure 4.14 shows the difference in detected peaks for all datasets. Figure 4.14a shows the difference in total number of detected peaks over time, and Figure 4.14b shows the average intensities of peaks around ring 111 for all datasets. Here it is clearly visible that the total number of peaks decrease faster for the dataset of 1120 °C due to grain coarsening, resulting in the lowest amount of peaks for this dataset at the end of the hold time. The increase in grain size of this dataset can be visible in Figure 4.14b. With lower deformation temperature, the rate of nucleation of new grains is typically faster than the rate of growth of the grains [30]. As an effect, the resulting final grain size after recrystallization is typically lower, while the number of grains can be higher. This is supported by the results plotted, as the average intensity of the peaks increase at a slower rate and reach lower values for the dataset of 1080 °C compared to the dataset of 1120 °C. Furthermore, this can explain why the number of peaks found for the dataset of 1080 °C converge to a greater value in Figure 4.14a compared to the dataset of 1120 °C.

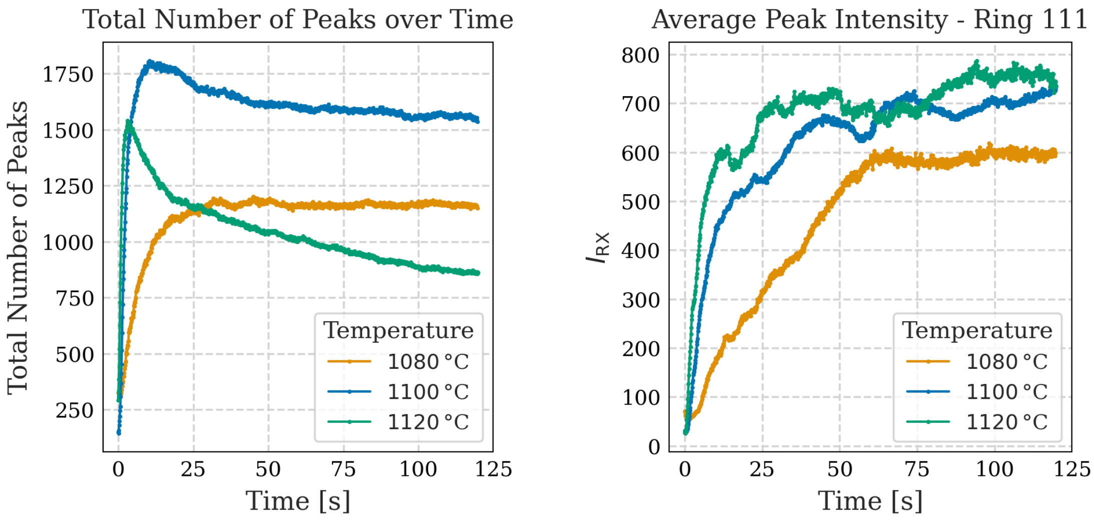

(a) **(b)**

Figure 4.14: Change in total number of peaks for all datasets in (a), and change in the average peak intensity along ring 111 for all datasets in (b).

4.4 Comparison with EBSD experiments

In this section, the computed results from the XRD data are compared to results from EBSD data obtained from Eriksson et al. [5]. For the EBSD results, the alloy samples were heated to 1080 °C for different strains of $\epsilon = [0.2, 0.4, 0.6]$. These samples were sectioned at the point of maximum bulge where the strain is the greatest, as demonstrated in Figure 4.15 (recreated from [22]). The scattered X-rays in the synchrotron measurements penetrate the sample, and thus represent the grains through the whole middle volume of the sample which the beam passes through. The average strain of the XRD data analysed is hence probably lower than the induced strain of 0.3. For this reason, the XRD results of strain 0.3 are compared to the EBSD results using a strain of 0.2. Note that the average strain in the XRD sample is still most probably lower than 0.2.

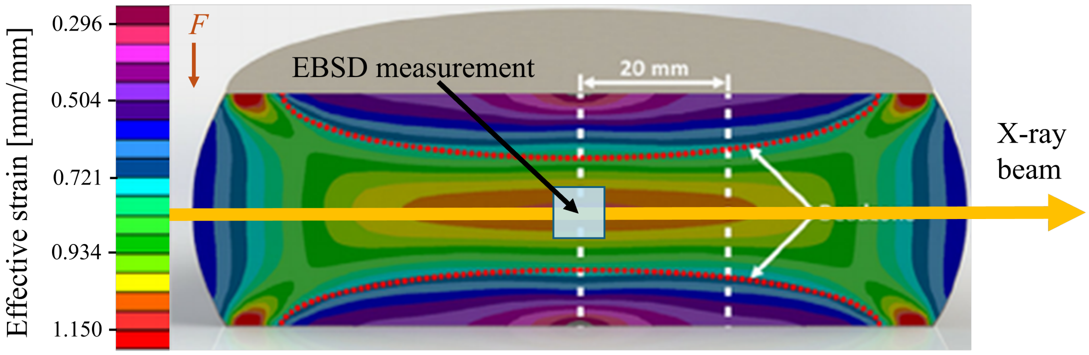

Figure 4.15: Example strain map of a forged Ni-based superalloy, showing the corresponding area analysed during the EBSD experiment, and the volume studied during the XRD experiment.

Figure 4.16 shows the comparison of f_{RX} between the XRD and EBSD results. As visible, the two curves follow the same shape, but differ in absolute magnitude. In the work of Eriksson et al., they showed that the kinetics of f_{RX} increase with increasing strain for the Haynes 282 alloy [5]. A greater strain in the area analysed during the EBSD measurements compared to the XRD measurements might thus explain the increase in magnitude between the two curves.

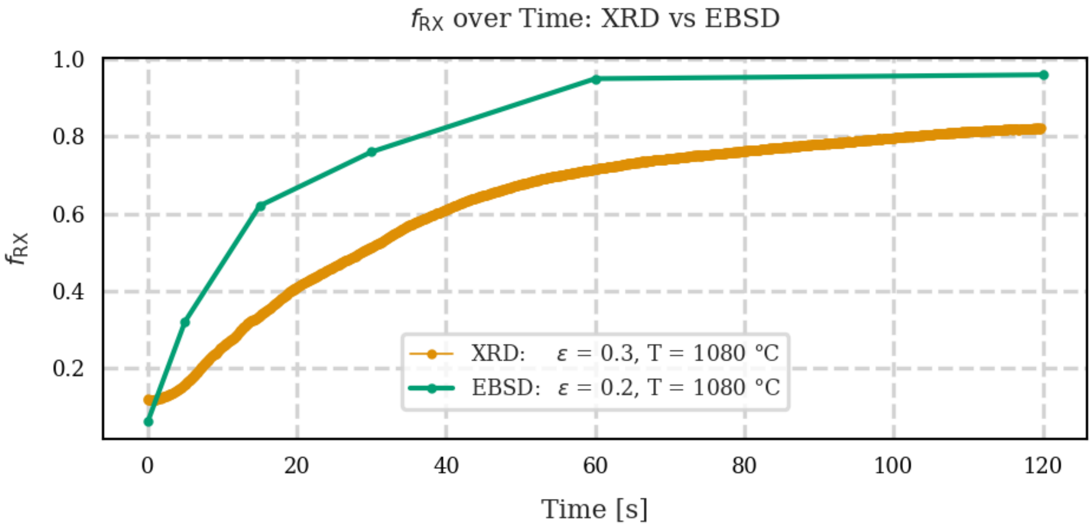

Figure 4.16: Comparison of f_{RX} over time between the XRD and EBSD measurements.

Figure 4.17 shows the difference in grain size evolution over time between the two methods. The EBSD results were obtained by measuring the average diameter of the grains, and the XRD by computing the average peak amplitude. As visible, both curves follow the same increasing shape. The EBSD results show a less continuous increase in grain size. A similar trend is visible in the XRD results when looking at the individual rings in Figure 4.13a, where the intensities from ring 200 and 220 show a more shifting rate of increment. Again it is important to note the uncertainties in the EBSD experiment. Different samples were measured for each time instance, such that there is uncertainty in the exact deformation temperature of the sample, the exact time instance studied, how the microstructure looked initially before the experiment, and if the quenching have affected the microstructure. These factors may also explain the less continuous shape of the EBSD results in Figure 4.17.

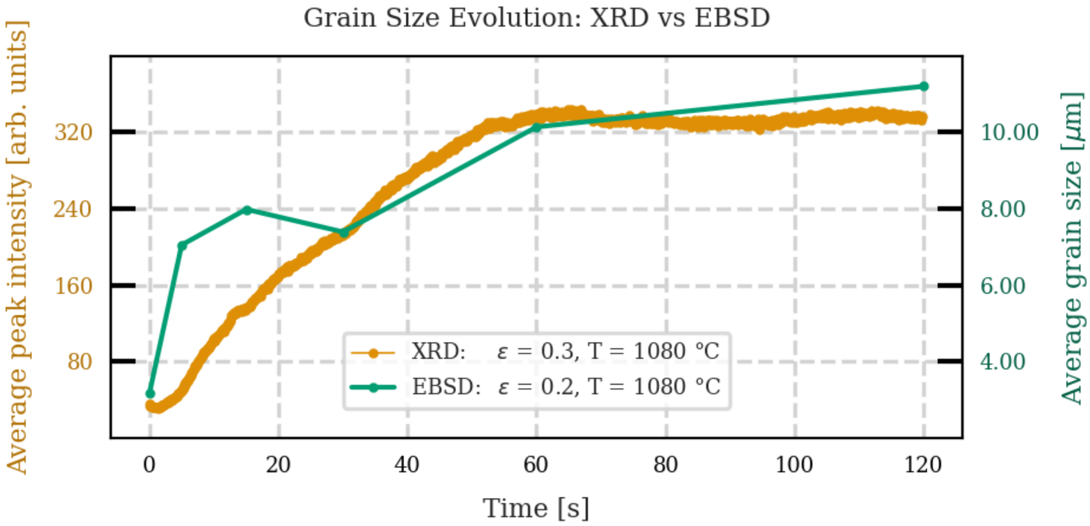

Figure 4.17: Comparison of grain size evolution over time between the XRD and EBSD measurements.

The peak intensities computed (representative of the grain sizes) show the average values over time. To get a better understanding of the complete set of the sizes at each time step, the distribution of peak intensities can be plotted. Figure 4.18 shows histograms of the probability density of the intensities of the peaks obtained in the XRD method (the same histograms used for Figure 4.5). Figure 4.18a shows the distribution at 0 s and Figure 4.18b at 120 s. Figure 4.19 shows histograms over the measured grain sizes in the EBSD images. A similar spread in the distribution can be observed for both methods, starting at a narrow distribution at 0 s, and becoming wider as the hold time progresses.

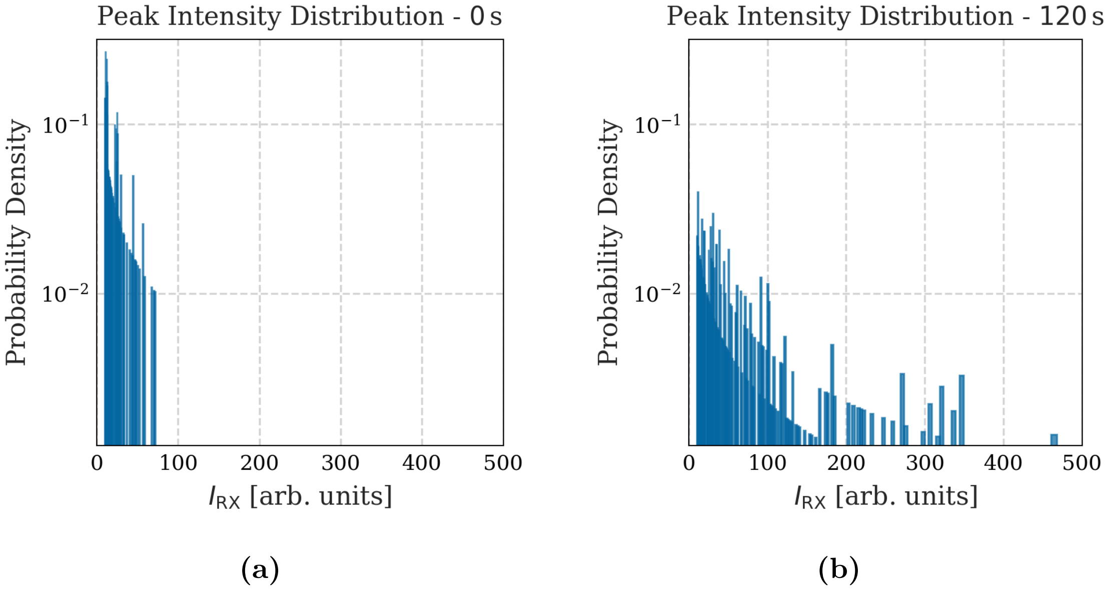

(a) **(b)**

Figure 4.18: Change in the distribution of peak intensities from the XRD results, (a) at 0 s and (b) at 120 s.

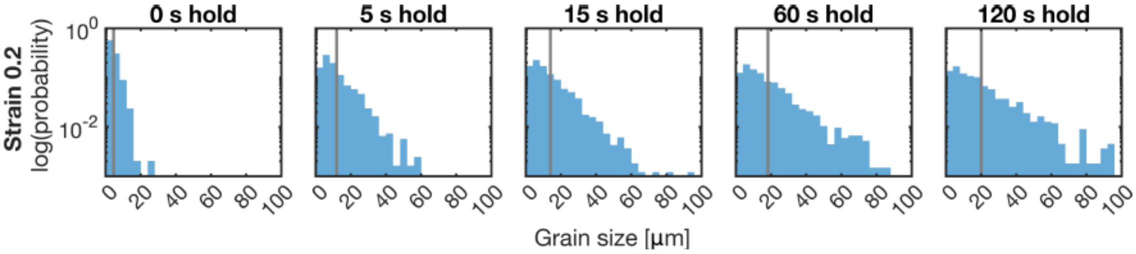

Figure 4.19: Change in the distribution of grain sizes measured from the EBSD images, ranging from 0 to 120 s hold time.

Figure 4.20 shows the change in number density over time. For the EBSD method, the number density is computed as the ratio between number of recrystallized grains and the total area of the sample analysed. The XRD equivalent is the number of detected peaks (note that the probed volume is constant over time). Both curves show a rapid increase in number density. The EBSD curve then reaches a maximum before decreasing again, whereas the XRD curve converges towards its maximum value. The EBSD maximum behaviour is also observed for the datasets of higher temperature, as visible in Figures 4.2b and 4.9b. Again, it is worth mentioning that the EBSD method looks at the area of maximum deformation whereas the XRD method shows the average over the probed volume.

Previous research on recrystallization of Ni-based superalloys suggest that pre-existing grains grow during mDRX, and that new grains can nucleate after an incubation time, typically on the order of several seconds to minutes [11][12]. As an example, Zouari et al. [10] used *in situ* EBSD to study mDRX in the Ni-based superalloy Inconel 718. Their samples were deformed at a temperature of 1020 °C, a strain rate of $0.1\,\mathrm{s}^{-1}$ and a strain of 0.25. They observed immediate growth of pre-existing grains after the deformation, as well as nucleation of new grains after an incubation time of over 30 seconds. As illustrated in Figure 4.20, this work, as well as the work by Eriksson et al., suggests that new grains nucleate immediately after the deformation without an incubation time. It might be that nucleation of new grains without incubation time is possible during mDRX. Another explanation could be that there exists small grains nucleated prior to the mDRX, that are too small to be resolved as individual peaks in the diffractogram. As these small grains begin to grow they become distinguishable, giving the impression of new grain nucleation, when in fact they had already been formed at an earlier stage. A more extensive study of diffraction from small grains is needed to evaluate this instant increase in number density.

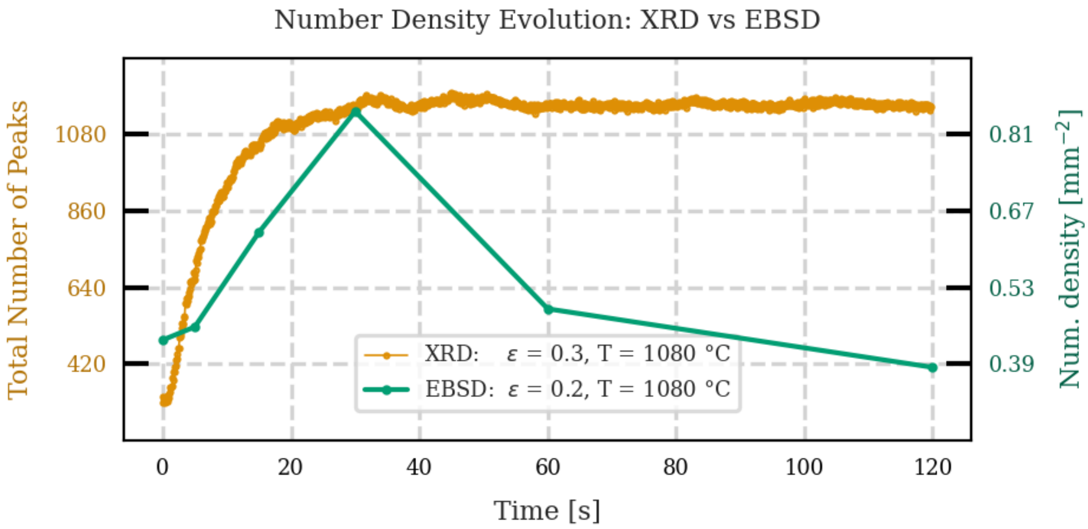

Figure 4.20: Comparison of number density over time between the XRD and EBSD methods.

5

Conclusion and outlook

This work has shown that *in situ* synchrotron XRD measurements can be used to effectively study mDRX. Prior to this study, no established method existed to separate the diffraction signal into contributions from deformed and recrystallized grains. In this work, a method to extract the deformed part of the signal was developed, enabling a quantitive analysis of the progression of the recrystallization over time. The method should be applicable to any crystalline material, opening up for high temporal resolution studies of recrystallization in various materials.

The computational methods were developed using data from deformation experiments of the Ni-based superalloy Haynes 282. A strain of 0.3, a strain rate of $0.05\,\mathrm{s}^{-1}$ and a temperature of 1100 °C were used during the deformation. Analysing this data provided insights into the dynamics of recrystallization in Haynes 282. The number of grains was seen to differ slightly between crystal orientations, which may be explained by the deformation texture as well as the difference in dislocation density throughout the sample. The evolution of grain size was also studied, by looking at the change in diffraction peak intensities over time, suggesting that the grains grew in size during the recrystallization. The recrystallization was also observed to be highly temperature dependent. The developed methods were applied to additional datasets using deformation temperatures of 1080 and 1120 °C, showing that the rate of recrystallization increased with temperature. Comparison with previous experimental EBSD measurements further supported the computed results, as they aligned with the conclusions drawn from the EBSD data. Altogether, this study not only advances the understanding of recrystallization in Haynes 282 but also establishes a robust framework for investigating recrystallization kinetics in other crystalline materials.

5.1 Future research

For future research, a more extensive study of the different parameters used in the computational methods, such as the influence of peak filtering parameters, can be made. This could potentially help avoid incorporating noise in the data analysis, and help capture peaks that might be missed. One limitation with the experimental technique is that it averages the signal over the entire probed volume. Since the degree of deformation varies throughout the sample, some regions may recrystallize faster than others. As a result, the diffracted signal represents an overall average of the recrystallization process, making it challenging to capture site-specific details.

This limitation could potentially be addressed through improved sample preparation methods.

This work focused on dDRX, having clear stages of nucleation and growth of grains. It remains to be seen whether this method is equally effective for cDRX, where the recrystallization instead occurs in a continuous manner by a gradual transformation of subgrains into new grains. It is also of interest to conduct a deeper study of the diffraction from small grains, in order to evaluate if the observed instant increase in number of peaks is due to nucleation of new grains or growth of existing small grains. One way of investigation this could be through using a machine learning model, trained on finding peaks or dots in experimental data. Training such model on a variety of datasets of different strain and deformation temperatures, especially from *in situ* data, could potentially make it generalizable to new experiments. In this way, data analysis of the number of peaks, or even extending to recrystallized fraction, could be computed live during the data collection simultaneous to a running experiment.

Bibliography

[1] Comission E. Reducing emissions from aviation;. Accessed: 2025-05-15.

[2] Gudivada G, Pandey AK. Recent developments in nickel-based superalloys for gas turbine applications. Journal of Alloys and Compounds. 2023;963:171128.

[3] 12 - Superalloys for gas turbine engines. In: Mouritz AP, editor. Introduction to Aerospace Materials. Woodhead Publishing; 2012. p. 251-67.

[4] International H. Haynes282;. Accessed: 2025-01-25.

[5] Eriksson E, Koeppe K, Hedström P, Jönsson S, Pettersson N. Meta-Dynamic Recrystallization in the Ni-Based Superalloy Haynes 282. Metals. 2023;13(8):1335.

[6] Mouritz AP. Introduction to Aerospace Materials. Woodhead Publishing Limited; 2012.

[7] Eriksson E. Dynamic and meta-dynamic recrystallization of Ni-based superalloy Haynes 282. Chalmers Tekniska Hogskola (Sweden); 2022.

[8] Huang K, Logé RE. A review of dynamic recrystallization phenomena in metallic materials. Materials & Design. 2016;111:548-74.

[9] Doherty R, Hughes D, Humphreys F, Jonas JJ, Jensen DJ, Kassner M, et al. Current issues in recrystallization: a review. Materials Science and Engineering: A. 1997;238(2):219-74.

[10] Zouari M, Logé RE, Bozzolo N. In Situ Characterization of Inconel 718 Post-Dynamic Recrystallization within a Scanning Electron Microscope. Metals. 2017;7(11):476.

[11] Nicolaÿ A, Bozzolo N, Grosdidier T, Hazotte A, Laigo J, Sauvage X. Influence of Strain Rate on Subsolvus Dynamic and Post-Dynamic Recrystallization Kinetics of Inconel 718. Acta Materialia. 2019;174:406-17.

[12] Qiao S, Liu Y, Liu Y, Zhang J, Xie X, Liu C, et al. Post-Dynamic Recrystallization Behavior of a Powder Metallurgy Ni-Co-Cr Based Superalloy under Different Deformation Conditions. Journal of Alloys and Compounds. 2022;898:162961.

[13] Dutta S, Verma N, Singh R, Ray RK. Microstructural evolution, recovery and recrystallization kinetics of isothermally annealed ultra low carbon steel. Materials Research Express. 2020;7(1):016554.

[14] Khan H, Uddin S, Raza W, Dhingra S, Shakoor A, Rehman AU, et al. Experimental methods in chemical engineering: X-ray diffraction spectroscopy—XRD. The Canadian Journal of Chemical Engineering. 2020;98(6):1255-66.

[15] Cornelius TW, Thomas O. Progress of in situ synchrotron X-ray diffraction studies on the mechanical behavior of materials at small scales. Progress in Materials Science. 2018;94:384-434.

[16] Science DP. How does a synchrotron radiation source work?;. Accessed: 2025-05-13.

[17] Couchet C, Geandier G, Teixeira J, Bonnet F, Allain SY. Ferrite Recrystallization Characterization by Isolated Diffraction Spot Tracking During High-Energy X-ray Diffraction Experiments. Metallurgical and Materials Transactions A. 2024:1-6.

[18] Moreno M, Fundenberger JJ, Bocher P, Hazotte A, Grosdidier T. Real-time investigation of recovery, recrystallization and austenite transformation during annealing of a cold-rolled steel using high energy X-ray diffraction (HEXRD). Metals. 2018;9(1):8.

[19] Humphreys FJ, Hatherly M. Deformation Textures. In: Humphreys FJ, Hatherly M, editors. Recrystallization and Related Annealing Phenomena. 2nd ed. Oxford: Elsevier; 2004. p. 67-89.

[20] DESY. P07 The High Energy Materials Science Beamline of Helmholtz-Zentrum Hereon and DESY;. Accessed: 2025-05-12.

[21] instruments T. DIL 805A/D;. Accessed: 2025-05-12.

[22] Buckingham RC, Rae CMF, Stone HJ. The effect of strain distribution on microstructural developments during forging in a newly developed nickel base superalloy. Materials Science and Engineering: A. 2016;654:317-28.

[23] Kieffer J, Karkoulis D. PyFAI, a versatile library for azimuthal regrouping. In: Journal of Physics: Conference Series. vol. 425. IOP Publishing; 2013. .

[24] Knudsen EB, Goret G, Kieffer J, Henningsson A, Svensson C, Thibault P. FabIO: easy access to two-dimensional X-ray detector images in Python. Journal of Applied Crystallography. 2013;46(2):537-9.

[25] Erb D. pybaselines: A Python library of algorithms for the baseline correction of experimental data. Zenodo; 2022.

[26] Serra J. Mathematical Morphology. In: Encyclopedia of Mathematical Geosciences. Cham: Springer International Publishing; 2023. p. 820-35.

[27] et al PV. SciPy 1.0: Fundamental Algorithms for Scientific Computing in Python. Nature Methods. 2020;17(3):261-72.

[28] Vila FD, Rehr JJ, Kelly SD, Bare SR, Kas JJ. Theoretical x-ray absorption Debye-Waller factors. Physical Review B—Condensed Matter and Materials Physics. 2007;76(1):014301.

[29] Song Y, Zhang Y, Wang B, Wang Y, Liang X, Zhang Y, et al. Hot Deformation and Recrystallization Behavior of a New Nickel-base Superalloy for Ultra-supercritical Applications. Journal of Materials Research and Technology. 2022;19:4308-24.

[30] Mittemeijer EJ. Recovery, Recrystallization and Grain Growth. In: Fundamentals of Materials Science: The Microstructure–Property Relationship Using Metals as Model Systems. Berlin, Heidelberg: Springer Berlin Heidelberg; 2011. p. 463-96.

DEPARTMENT OF PHYSICS
CHALMERS UNIVERSITY OF TECHNOLOGY
Gothenburg, Sweden
www.chalmers.se